ACS APPLIED BIO MATERIALS

www.acsabm.org Article

Electrospun Magnetic Composite Poly-3-hydroxybutyrate/Magnetite Scaffolds for Biomedical Applications: Composition, Structure, Magnetic Properties, and Biological Performance

Artyom S. Pryadko A, Yulia R. Mukhortova, Roman V. Chernozem, Igor Pariy, Svetlana I. Alipkina, Irina I. Zharkova, Andrey A. Dudun, Vsevolod A. Zhuikov, Anastasia M. Moisenovich, Garina A. Bonartseva, Vera V. Voinova, Dariana V. Chesnokova, Alexey A. Ivanov, Daria Yu. Travnikova, Konstantin V. Shaitan, Anton P. Bonartsev, Dmitry V. Wagner, Lada E. Shlapakova, Roman A. Surmenev,* and Maria A. Surmeneva*

Cite This: *ACS Appl. Bio Mater.* 2022, 5, 3999−4019 Read Online

ACCESS | Metrics & More | Article Recommendations | Supporting Information

ABSTRACT: Magnetically responsive composite polymer scaffolds have good potential for a variety of biomedical applications. In this work, electrospun composite scaffolds made of polyhydroxybutyrate (PHB) and magnetite (Fe_3O_4) particles (MPs) were studied before and after degradation in either PBS or a lipase solution. MPs of different sizes with high saturation magnetization were synthesized by the coprecipitation method followed by coating with citric acid (CA). Nanosized MPs were prone to magnetite−maghemite phase transformation during scaffold fabrication, as revealed by Raman spectroscopy; however, for CA-functionalized nanoparticles, the main phase was found to be magnetite, with some traces of maghemite. Submicron MPs were resistant to the magnetite−maghemite phase transformation. MPs did not significantly affect the morphology and diameter of PHB fibers. The scaffolds containing CA-coated MPs lost 0.3 or 0.2% of mass in the lipase solution and PBS, respectively, whereas scaffolds doped with unmodified MPs showed no mass changes after 1 month of incubation in either medium. In all electrospun scaffolds, no alterations of the fiber morphology were observed. Possible mechanisms of the crystalline-lamellar-structure changes in hybrid PHB/Fe_3O_4 scaffolds during hydrolytic and enzymatic degradation are proposed. It was revealed that particle size and particle surface functionalization affect the mechanical properties of the hybrid scaffolds. The addition of unmodified MPs increased scaffolds' ultimate strength but reduced elongation at break after the biodegradation, whereas simultaneous increases in both parameters were observed for composite scaffolds doped with CA-coated MPs. The highest saturation magnetization—higher than that published in the literature—was registered for composite PHB scaffolds doped with submicron MPs. All PHB scaffolds proved to be biocompatible, and the ones doped with nanosized MPs yielded faster proliferation of rat mesenchymal stem cells. In addition, all electrospun scaffolds were able to support angiogenesis in vivo at 30 days after implantation in Wistar rats.

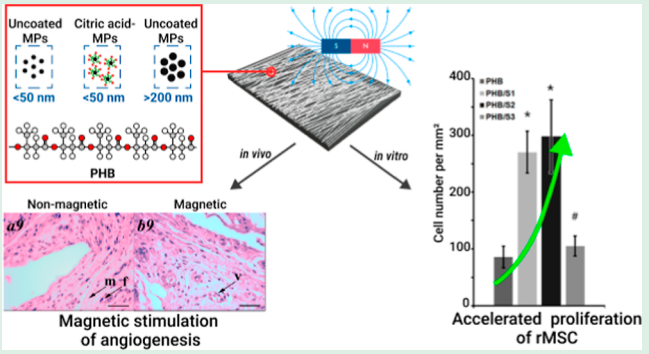

KEYWORDS: *magnetite, composite scaffold, poly-3-hydroxybutyrate, electrospinning, magnetization*

1. INTRODUCTION

Magnetically active scaffolds are a promising class of stimuli-responsive materials for biomedical applications and enable noninvasive targeted and controlled stimulation of the cell or tissue (after implantation) via an external magnetic field. External magnetic stimuli can be controlled temporally and spatially allowing for precise control over a cellular response. In a recent study, it has been shown that mouse preosteoblast cell attachment and osteogenic differentiation were significantly improved using nanocomposites of poly(lactide-*co*-glycolide) and oleic acid-modified iron oxide nanoparticles in the presence of an external static magnetic field.[1] In another work, magnetic nanocomposites consisting of a poly(ε-caprolactone) matrix and magnetite nanoparticles enhanced adhesion, proliferation, and differentiation of human mesen-

Received: June 10, 2022
Accepted: July 20, 2022
Published: August 4, 2022

https://doi.org/10.1021/acsabm.2c00496
ACS Appl. Bio Mater. 2022, 5, 3999−4019

chymal stem cells under exposure to a time-dependent magnetic field.[2]

Magnetically responsive biomaterials are usually obtained via the incorporation of magnetic agents into biocompatible matrices.[3] Magnetic agents usually consist of pure metals, metal alloys, or metal oxides. Particles composed of a pure metal (Fe, Co, or Ni) usually have stronger magnetic properties as compared to metal oxides.[4] Despite high magnetization, pure-metal particles are sensitive to oxidation, which in turn deteriorates their magnetic properties. Moreover, pure-metal particles of Co or Ni are not appropriate for biomedical applications because these particles are toxic.[5] Among various metal oxide magnetic agents, superparamagnetic magnetite (Fe_3O_4) and maghemite (γ-Fe_2O_3) are commonly used due to their unique physiochemical properties, good intrinsic magnetic characteristics, chemical stability under physiological conditions, and biocompatibility.[6] Magnetite particles (MPs) have the strongest magnetism among known transition-metal oxides.[7] In light of the above, MPs are promising candidates for a magnetic filler in magnetic composite scaffolds. The colloidal stability of MPs plays an important role in their biomedical applications.[8] Uncoated MPs tend to aggregate; therefore, functionalization with a surfactant is needed to improve their stability. Citric acid (CA)-functionalized negatively charged particles are more stable in aquatic systems.[9] CA, which contains three −COOH groups, can be easily adsorbed onto the surface of MPs: one or two carboxylate moieties can be chemisorbed, leaving at least one free carboxyl group on the particle surface, making it hydrophilic and preventing particle agglomeration.[10] Therefore, in the present study, CA-coated and uncoated MPs and MPs of different sizes were investigated.

Various approaches have been utilized to synthesize scaffolds with magnetic particles incorporated into polymeric matrices, for example, electrospinning,[11] dip coating,[12] solvent casting/particle leaching,[13] and freeze drying.[14] Electrospinning is a versatile and effective method for the production of polymeric fibrous scaffolds with properties required for biomedical applications, for example, a high surface area/volume ratio, small interfibrous pore size with high porosity, and vast possibilities for surface functionalization.[15] These properties ensure desirable cell attachment and oxygen and/or nutrient transport.[16]

Polyhydroxybutyrate (PHB) is a piezoelectric, thermoplastic, biocompatible, and biodegradable polymer of the polyhydroxyalkanoate family and is produced by various microorganisms. Biodegradable scaffolds made of PHB can support long-term tissue regeneration owing to a slow degradation rate.[17] A degradation product of PHB called D-3-hydroxybutyric acid is a natural constituent of human blood that is nontoxic in bodily fluids and exerts no inflammatory effects.[18] Thus, PHB/magnetite electrospun scaffolds are promising magnetic biomaterials for tissue engineering applications. To the best of our knowledge, there are only a few research articles on such composite scaffolds.[19,20] Furthermore, these reports are not focused on the changes in structure occurring in PHB upon the addition of MPs; the scaffolds in these studies possess low magnetization. Given that the preparation of hybrid scaffolds is a two-stage process—that is, MP synthesis and scaffold fabrication—it is important to investigate how the synthesis route of the particles will affect their properties, in particular during the electrospinning process.

In this study, MPs were synthesized using three routes. We evaluated the influence of the particle synthesis route on their subsequent usefulness as fillers in a polymer matrix. Thus, the aim of this work was to obtain PHB/magnetite electrospun scaffolds with high saturation magnetization by means of three types of MPs. As a result, a biocompatible electrospun composite scaffold was developed, with the highest magnetization among all known analogues. The effects of MPs on the growth of lamellae and on the structure of PHB were researched as well.

2. MATERIALS AND METHODS

2.1. Materials. Hydrochloric acid (HCl), CA ($C_6H_8O_7$), ferric(III) chloride hexahydrate ($FeCl_3{\cdot}6H_2O$), ferrous(II) sulfate heptahydrate ($FeSO_4{\cdot}7H_2O$), sodium hydroxide (NaOH), ammonium hydroxide (NH_4OH), urea [$(NH_2)_2CO$], and poly(3-hydroxybutyrate) (PHB) of natural origin were purchased from Sigma-Aldrich. Only deionized water was used in in vitro experiments.

2.2. Preparation and Characterization of Composite Electrospun PHB/Magnetite Scaffolds. *2.2.1. Synthesis of MPs.* MPs were synthesized by the coprecipitation method via one of three procedures. The first one included heating up to 60 °C, followed by coating the MPs with a surfactant. The second one included the synthesis of MPs at room temperature with a pH shift to 2 beforehand.[21] In the third synthesis route, the preparation of magnetite also involved heating but at higher temperatures, exceeding the decomposition temperature of urea.

The first synthesis route can be described by the following reaction

$$2FeCl_3 + FeSO_4 + 8NaOH \rightarrow Fe_3O_4 + 6NaCl + Na_2SO_4 + 4H_2O \quad (1)$$

Ferric(III) chloride hexahydrate (3.73 g) and ferrous(II) sulfate heptahydrate (1.92 g) were loaded into a three-necked flask, which was placed on a magnetic stirrer and connected to the Schlenk system. Dry salts were degassed in vacuum and saturated with argon three times. Then, 175 mL of deionized water was introduced into the flask, followed by mixing and heating on the magnetic stirrer. The solution was heated to 60 °C with stirring at 300 rpm for 30 min. When 60 °C was reached, the stirring speed was raised to 1500 rpm, and 50 mL of 1.5 M NaOH was added dropwise into the solution with a syringe to shift pH to 11. At the same time, blackening of the solution was observed, which indicates magnetite formation. Heating was continued for 30 min.

To reduce aggregation of MPs, after 30 min of continuous heating, 3.7 mL of 50% (w/v) CA was introduced into the solution, and the temperature was increased to 80 °C with continuous stirring for 90 min. Next, the solution was decanted, and the powders were washed with deionized water. The washing procedure was repeated until a neutral pH was attained, and then the powders were precipitated by an external magnetic field and dried at 35 °C in a convection oven for 2 days. As a result, black magnetite powders were obtained. By this technique, a sample denoted S1 was synthesized. A schematic representation of the synthesis route for the S1 nanoparticles is shown in Figure 1.

In the second synthesis route, MPs were generated according to the following reaction

$$2FeCl_3 + FeSO_4 + 8NH_4OH \rightarrow Fe_3O_4 + 6NH_4Cl + (NH_4)_2SO_4 + 4H_2O \quad (2)$$

Ferric(III) chloride hexahydrate (2.80 g) and ferrous(II) sulfate heptahydrate (1.92 g) were placed in a three-necked flask and dissolved in 25 mL of deionized water, and the solution was mixed on the magnetic stirrer for 1 h at 300 rpm without heating. After that, a few drops of HCl were added to shift the pH to 1−2, followed by heating at 85 °C for 45 min. Then, the solution was cooled down to room temperature. At the next step, the rotation speed was raised to

https://doi.org/10.1021/acsabm.2c00496
ACS Appl. Bio Mater. 2022, 5, 3999−4019

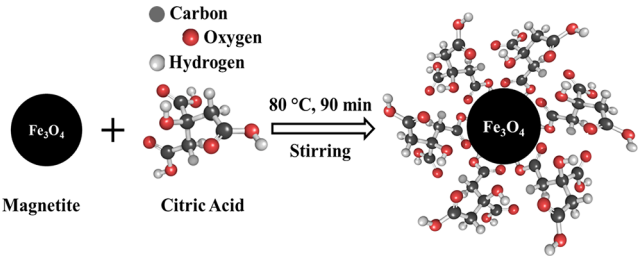

Figure 1. Schematic representation of the synthesis of CA-coated nanoparticles.

1500 rpm, and 8 mL of concentrated NH_4OH was added dropwise until pH 11 was reached. A color change from light orange to black was observed, indicating the formation of magnetite. After that, the reaction mass was incubated with stirring for 60 min. The resulting particles were precipitated and washed with deionized water. The particles were separated by magnetic separation and dried at 35 °C for 2 days in a convection oven. By this technique, a sample named S2 was obtained.

For the third synthetic procedure, 3.378 g of ferric(III) chloride hexahydrate, 1.713 g of ferrous(II) sulfate heptahydrate, and 6 g of urea were loaded into a three-necked flask with a connected reflux condenser. Then, 50 mL of deionized water was added with constant mixing on the magnetic stirrer at 300 rpm for 10 min. The solution was next heated to 115 °C for 18 h with stirring at 800 rpm and then cooled to room temperature. A precipitate was obtained by magnetic separation and washed with deionized water until a neutral pH was attained. The sample was dried at 35 °C in a convection oven for 2 days. The synthesis process can be described by the following equations

$$(NH_2)_2CO + H_2O \rightarrow 2NH_3 + CO_2 \quad (t > 85\ ^\circ C) \tag{3.1}$$

$$NH_3 + H_2O \rightarrow NH_4 + OH^- \tag{3.2}$$

$$Fe^{3+} + 3OH^- \rightarrow Fe(OH)_3 \tag{3.3}$$

$$Fe(OH)_3 \rightarrow FeOOH + H_2O \tag{3.4}$$

$$Fe^{2+} + 2OH^- \rightarrow Fe(OH)_2 \tag{3.5}$$

$$2FeOOH + Fe(OH)_2 \rightarrow Fe_3O_4 + 2H_2O \tag{3.6}$$

At the beginning of the reaction, yellow precipitates were observed, indicating the formation of $Fe(OH)_3$ as a consequence of Fe^{3+} hydrolysis. After 8 h, the color of the reaction system began to darken, and after 10 h, it turned black, which indicates the formation of Fe_3O_4. When a solution containing Fe^{2+} and Fe^{3+} and dissolved urea is heated to temperatures above 70 °C, urea decomposes into CO_2 and NH_3 (eq 3.1). Under reflux conditions, CO_2 leaves the system, and therefore, only NH_3 reacts with water to form hydroxyl ions (eq 3.2). With increasing pH, $Fe(OH)_3$ precipitates first (eq 3.3). $Fe(OH)_3$ next converts to FeOOH (eq 3.4), known as goethite. Once enough hydroxyl ions have formed, $Fe(OH)_2$ begins to precipitate (eq 3.5). Furthermore, magnetite is formed from the available FeOOH and $Fe(OH)_2$ nuclei (eq 3.6). By this approach, a sample designated as S3 was produced.

2.2.2. Fabrication of PHB/Magnetite Composites Using Electrospinning. Dry PHB polymer powder (natural origin, Sigma-Aldrich) was dissolved in chloroform to achieve a concentration of 6 wt % and was employed as a control. For PHB/MP composites, MPs (S1, S2, or S3) in an amount of 8 wt % by weight of the polymer were dispersed in chloroform ($CHCl_3$, Sigma-Aldrich) and sonicated (Scientz-IID, Ningbo SCienta Biotechnology Co. Ltd., China) for 2 h at room temperature. Then, 6 wt % of dry PHB polymer powder was added to the Fe_3O_4 suspension and placed on the magnetic stirrer at 400 rpm and 60 °C for 2 h incubation. Pure PHB and PHB/MP composite scaffolds were electrospun at a collector rotation speed of 200 rpm, a 9 kV voltage, and a 0.9 mL/h flow rate. The MPs and electrospun scaffolds were prepared, and their abbreviations were assigned as follows and used throughout the study (Table 1).

Table 1. Types of the Analyzed Composites and Their Abbreviated Names

sample	abbreviation
Fe_3O_4 (Ar with CA)	S1
Fe_3O_4 (nitrogen)	S2
Fe_3O_4 (ammonia)	S3
PHB/Fe_3O_4 (Ar with CA)	PHB/S1
PHB/Fe_3O_4 (nitrogen)	PHB/S2
PHB/Fe_3O_4 (ammonia)	PHB/S3

2.3. Characterization of the Scaffolds. The morphology of the MPs and electrospun fibrous scaffolds was examined under a scanning electron microscope (Quanta 600, Thermo Fisher, Japan). The diameters of the particles and fibers were calculated using the ImageJ software using the resultant scanning electron microscopy (SEM) images.

The phase composition was characterized by X-ray diffraction (XRD) analysis on a Shimadzu XRD 7000S diffractometer equipped with a high-speed 1280-channel OneSight detector using Cu Kα radiation (λ = 1.5406 Å) at a scan rate of 4°/min and a step size of 0.02° in a 2θ Bragg−Brentano geometry. The XRD patterns were recorded in the 2θ range from 5 to 80°. The crystallite size D_{hkl} was estimated according to Scherrer's equation

$$D_{hkl} = \frac{K\lambda}{\beta \cos\theta} \tag{4}$$

where λ is the X-ray wavelength, β means peak width at half-height, K represents a dimensionless particle shape factor (usually set to 0.9[22]), and θ denotes the diffraction angle.

The dislocation density δ was calculated as follows

$$\delta = \frac{1}{D^2} \tag{5}$$

The microstress ε was estimated according to the equation

$$\varepsilon = \frac{\beta}{4 \tan\theta} \tag{6}$$

Raman spectra and optical photographs were obtained using a confocal Raman microscope coupled with the scanning probe optical unit (NTEGRA Spectra, NT-MDT, Russia) equipped with a 100× objective. Excitation was performed with a semiconductor laser at a wavelength of 633 nm with a maximum power of 50 mW. To prevent heating of the sample and phase transformations, only 1% of the laser power was applied.

Differential scanning calorimetry (DSC) was performed on a DSC Q2000 instrument in the range of 50−250 °C in a nitrogen atmosphere at a heating rate of 10 °C/min. Crystallinity (X_c) of the pure PHB scaffold and the PHB composite with magnetite was evaluated by means of the formula

$$X_c = \frac{\Delta H_f}{\Delta H_f^0} \bullet 100\% \tag{7}$$

where ΔH_f is the heat of fusion ($J \cdot g^{-1}$) and the heat of fusion for 100% crystalline PHB (ΔH_f^0) is 146 $J \bullet g^{-1}$.[23]

The mechanical properties of the electrospun fibrous pure scaffolds and composites were evaluated in ambient air at room temperature using an Instron 3369 universal testing machine (Instron, United States). Samples with an average thickness of 0.2 mm were cut out in a rectangular shape with a length of 50 mm and a width of 10 mm.

The magnetic properties of MPs and electrospun composite scaffolds were investigated at a temperature of 300 K with an external pulsed magnetic field of 0−6.5 kOe on a pulsed magnetometer. The

https://doi.org/10.1021/acsabm.2c00496
ACS Appl. Bio Mater. 2022, 5, 3999−4019

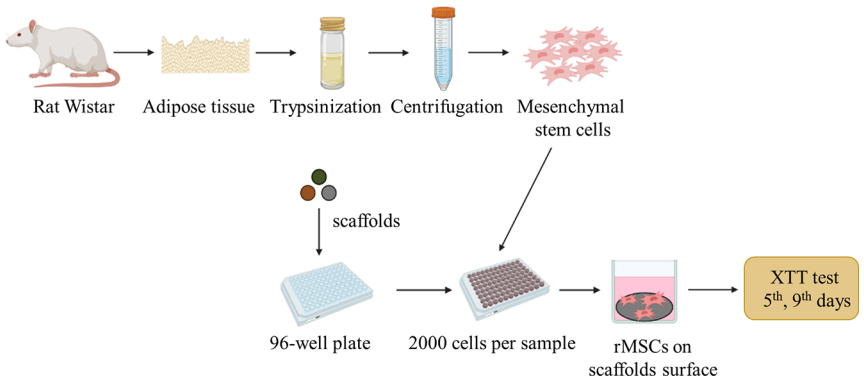

Figure 2. Outline of the assay of rMSC viability.

measurements were carried out according to the method described elsewhere.[24]

2.4. Enzymatic and Nonenzymatic Hydrolytic Degradation. Nonenzymatic degradation of scaffolds PHB, PHB/S1, PHB/S2, and PHB/S3 was conducted in phosphate-buffered saline [PBS; Merck (formerly Sigma-Aldrich), Darmstadt, Germany] at pH 7.4. For enzymatic degradation, lipase was added to PBS to a concentration of 0.25 mg/mL as previously described.[25] For a short period, all solutions were stored in a shaker−incubator (37 °C, 150 rpm). To maintain buffer quality, lipase-free PBS and lipase-containing PBS were refreshed every 3 days. The films of materials were examined after incubation for 30 days. To prevent bacterial contribution to the polymer degradation, sodium azide (2 g/L) was added to the buffer.

2.5. Biocompatibility Evaluation of Scaffolds In Vitro and In Vivo. *2.5.1. In Vitro Cell Viability Assay.* For rat mesenchymal stem cells (rMSCs), attachment to and growth on scaffolds were assessed by a biochemical assay using a tetrazolium chloride (XTT) cell proliferation kit (Biological Industries, Israel). rMSCs were isolated from the fat tissue of young (3−5 days old) Wistar rats, cultured for 2 weeks in Dulbecco's modified Eagle's medium (PanEco, Russia) supplemented with 10% of fetal calf serum (Biological Industries, Israel) and 100 U/mL penicillin, and characterized by means of mesenchymal-stem-cell phenotype markers (CD90, CD29, CD45, and CD11b/c; eBioscience, USA) on a flow cytometer (FACS ARIA II, USA) as described elsewhere.[26]

The cells were cultured on the scaffolds' surface in the alpha-MEM medium (PANEKO, Russia) containing 10% of fetal bovine serum (HyClone, USA), 100 IU/mL penicillin, and 100 μg/mL streptomycin (PANEKO) at 37 °C in an atmosphere containing 5% of CO_2; the medium was refreshed every 3 days. Scaffolds 5 × 5 mm^2 (n = 6) were placed in the wells of a 96-well plate, and the cell suspension was applied from above at 2000 cells per sample. The XTT assay was conducted in accordance with the manufacturer's protocol. The measurement was carried out on days 5 and 9 of cell cultivation. A schematic representation of the biological assay is shown in Figure 2.

2.5.2. Scanning Electron Microscopy. The cells were cultured on scaffolds for 1 week as described in Section 2.5.1. For SEM analysis, the samples of materials were washed twice in PBS. The cells were fixed overnight in a fixative mixture (2% formalin and 2.5% glutaraldehyde in phosphate buffer). The fixed samples were buffered three times and dehydrated in a graded series of ethanol solutions in washing buffer: 30, 50, 70, 82, and 96%. The samples were incubated in each solution twice for 5 min. The samples were then washed twice with a mixture of 96% ethanol and hexamethyldisilazane (HDMS) in a 1:1 ratio and then with pure HDMS. After that, the matrices were kept in a small volume of HDMS until complete evaporation. The dehydrated samples were coated with a thin layer of platinum on a spray device (IB3, GIKO, Japan). The sputtered samples were examined under a TM3000 scanning electron microscope (Hitachi, Japan).

2.5.3. Fluorescence Microscopy. By day 7 of culturing on PHB, PHB/S1, PHB/S2, or PHB/S3, rMSCs were fixed with 4% paraformaldehyde in saline for 30 min at room temperature in the dark, followed by washing thrice in saline. Then, the cells were permeabilized with 0.1% Triton X-100 in saline for 10 min at 4 °C and washed twice with saline containing 0.1% of fetal bovine serum. To visualize the actin cytoskeleton, the cells were incubated with phalloidin conjugated with trimethylrhodamine (TRITC) (Sigma-Aldrich, Darmstadt, Germany), as recommended by the manufacturer, and washed three times with saline. Hoechst 33342 (Thermo Fisher Scientific, Waltham, MA, USA; 1 μg/mL) was added to counterstain the nuclei. The samples were examined under a Nikon Ti-E microscope with confocal module A1 and an Apo TIRF Plan Fluor 63 × 1.49 objective. Images were acquired using an Eclipse Ti-E microscope with confocal module A1 (Nikon Corporation, Japan).

2.5.4. Laboratory Animals and Surgical Operations. Surgical instruments (Kocher clamps, surgical tweezers, scissors, hooks, and eye scissors; Medtechnika, Kazan, Russia), ethyl alcohol, a 0.9% sodium chloride solution (saline), nitrofurazone, surgical Dacron sutures, bandages, hygroscopic medical cotton wool, gloves, syringes, 2,4,6-trinitrobenzenesulfonic acid, Zoletil 100, xylazine, a 10% formaldehyde solution, and wipes were acquired from commercial sources. All the experiments and surgical procedures complied with the ISO 10993-1:2009 ethical guidelines and were approved by the Bioethics Committee of the Faculty of Biology, M.V. Lomonosov Moscow State University (decision # 16.1 of May 28, 2021). The experiment was conducted on 12 male white Wistar rats (weight 300 ± 50 g, aged 2 months). The animals were kept under standard conditions on a 12 h/12 h light/dark cycle, with free access to water and feed. Immediately before implantation of the scaffolds, each animal was anesthetized with Zoletil 100 (Virbac, France) at a dose of 5 mg/kg in combination with the muscle relaxant xylazine (Bioveta, Czech Republic) at a dose of 6 mg/kg intramuscularly.[27] Next, all 12 Wistar rats were distributed into three groups of four males for implantation of scaffolds for various periods: 7, 14, or 30 days. Scaffolds PHB/S1, PHB/S2, and PHB/S3 were implanted subcutaneously into the abdominal area of rats. On the 7th, 14th, and 30th days after the scaffold implantation, the rats were euthanized by an anesthesia overdose. Following the euthanasia, the implantation area was opened; tissues from the connective-tissue capsule (that formed around the implanted samples) along with a small amount of surrounding tissues were excised for an analysis of the tissue response by histological methods. The explants were prepared in the form of a neatly cut capsule, marked, wrapped in a medical gauze bandage, immersed in a 10% neutral buffered formaldehyde solution (pH 7.4), and fixed for 24 h.

2.5.5. Histological Analysis. This analysis of the excised samples was carried out next. The samples were fixed in 70% ethanol for 24−72 h. After that, they were washed, dehydrated, and submerged in methylmethacrylate (Osteo-Bead; Sigma-Aldrich [Merck], Germany) with subsequent polymerization according to the standard procedure recommended by the manufacturer. The resultant blocks were used to prepare primary slices 200 μm in thickness (low-speed sow jet; Switzerland), which served for making secondary slices 40−50 μm

https://doi.org/10.1021/acsabm.2c00496
ACS Appl. Bio Mater. 2022, 5, 3999−4019

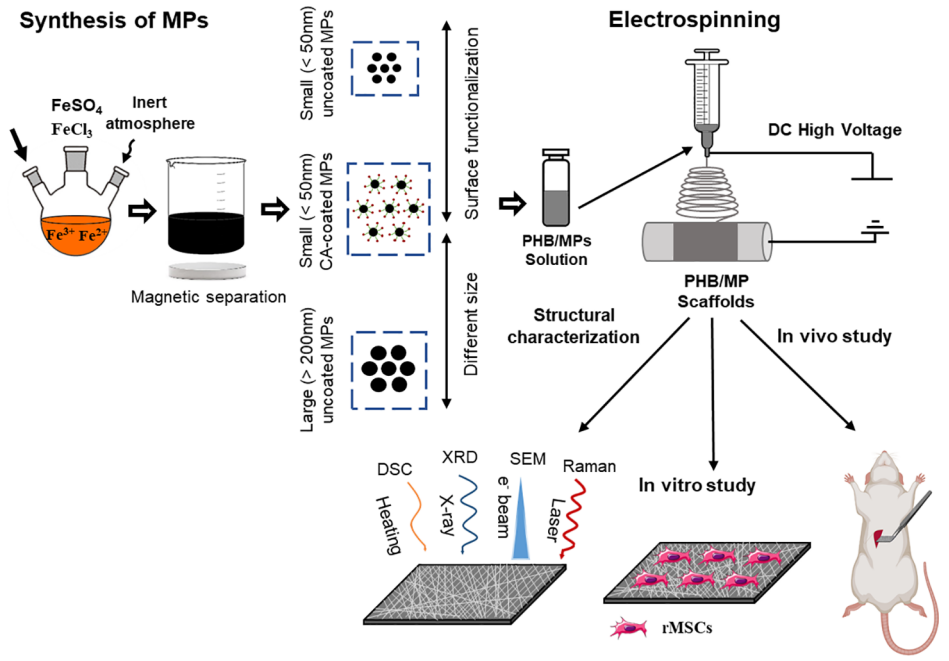

Figure 3. Schematic representation of the fabrication and characterization of electrospun composite PHB/Fe_3O_4 scaffolds.

thick. Slice thickness control was implemented using a standard mechanical drum-type micrometer.[27]

Microscopic examination was carried out under a Biomed 1 Var.2 fluorescent imaging microscope (Biomed, Russia) with a MYscope 300M digital ocular (Webbers, Taiwan). Up to 10 images (3132 × 2325 pixels) of each sample at 10× and 40× magnification were captured and digitized. The fields of view were all tangential to the material.

2.6. Statistical Analysis. The nonparametric Kruskal–Wallis test was employed for the statistical evaluation of data using the SPSS/PC + Statistics 12.1 software package (SPSS). The data are presented as the mean ± standard error of the mean and were considered significant at $p < 0.05$.

3. RESULTS AND DISCUSSION

The study concept is illustrated in Figure 3. MPs with different sizes and surface functionalization were obtained via one of the three synthesis routes. Incorporation of the synthesized MPs into the PHB matrix and fabrication of hybrid PHB/Fe_3O_4 composite scaffolds by the electrospinning technique were performed next. We evaluated the influence of the particle synthesis route on the subsequent suitability of the scaffolds as fillers in a polymer matrix. To determine the effect of MP incorporation on the morphology, crystalline structure, and biological performance of the fibers, PHB/Fe_3O_4 composite scaffolds were thoroughly investigated using different characterization techniques.

3.1. Characterization of the Fe_3O_4 Particles. Figure 4 presents SEM images (A–C) and size distributions (D–F) of the MPs generated via various synthesis routes. There was no significant difference in particle size between S1 and S2 samples: the particle size was 47 ± 9 and 46 ± 8 nm, respectively. The size of S3 particles was 280 ± 80 nm, which can be attributed to the longer synthesis time as compared to S1 and S2 nanoparticles.

Figure 4G shows XRD results on the MPs fabricated via different approaches. The samples yielded peaks at 30.35, 35.63, 43.49, 53.56, 57.12, and 62.81°, corresponding to D_{hkl} crystalline planes (220), (311), (400), (422), (511), and (440) of magnetite, in good agreement with the standard pattern of magnetite (ICDD PDF card no. 01-080-6403). The quantitative analysis revealed pure-phase magnetite in all the MPs synthesized in this study. Due to the cubic symmetry of MPs, the average crystallite size can be computed via Scherrer's equation from the full width at half-maximum of diffraction peaks. Thus, the crystallite size (D) for S1, S2, and S3 was 13 ± 1, 13 ± 1, and 30 ± 3 nm, respectively. Identifying magnetite and maghemite using only XRD analysis can be quite challenging because both have spinel-type structures and similar lattice parameters (0.8350 nm for γ-Fe_2O_3 and 0.8396 nm for Fe_3O_4).[28] Therefore, Raman spectroscopy was also used here, and the recorded spectra of MPs are presented in Figure 4H. A Raman spectrum of the S3 sample features the shifts characteristic for magnetite: ∼670 cm^{-1} (Fe–O symmetrical stretching), 540 cm^{-1} (Fe–O asymmetrical bending), and 310 cm^{-1} (Fe–O symmetrical bending). No peaks of other iron oxides were observed; therefore, only pure-phase magnetite formed in our procedures. For samples S1 and S2, three additional peaks of maghemite were seen at 380, 460, and 510 cm^{-1}, which were assigned to Fe–O asymmetric bending vibrations.

Magnetic properties of the prepared MPs were assayed next, and the obtained magnetization curves of the Fe_3O_4 particles are given in Figure 5.

The saturation magnetization (σ_s) of samples S1 and S2 was 64.1 ± 0.1 and 69.1 ± 3.7 emu/g, respectively. The presence of the maghemite phase in the samples led to a decrease in σ_s. Magnetite is a ferrimagnetic material with a spinel-facing crystal structure. Its tetrahedral positions are occupied by Fe^{3+}, while octahedral positions are occupied by Fe^{3+} and Fe^{2+}, and its $\sigma_s \approx 92–100$ emu/g.[29] Maghemite, γ-Fe_2O_3, also has inverse spinel structure but features mostly Fe^{3+} and cationic vacancies at octahedral positions; accordingly, it has lower saturation magnetization: ∼50–80 emu/g.[29,30] S1 has slightly lower σ_s due to the presence of the CA surface layer. Sample S3 has the highest saturation magnetization, 107.5 ± 5.1 emu/g, due to the purity of phase composition and the larger

https://doi.org/10.1021/acsabm.2c00496
ACS Appl. Bio Mater. 2022, 5, 3999–4019

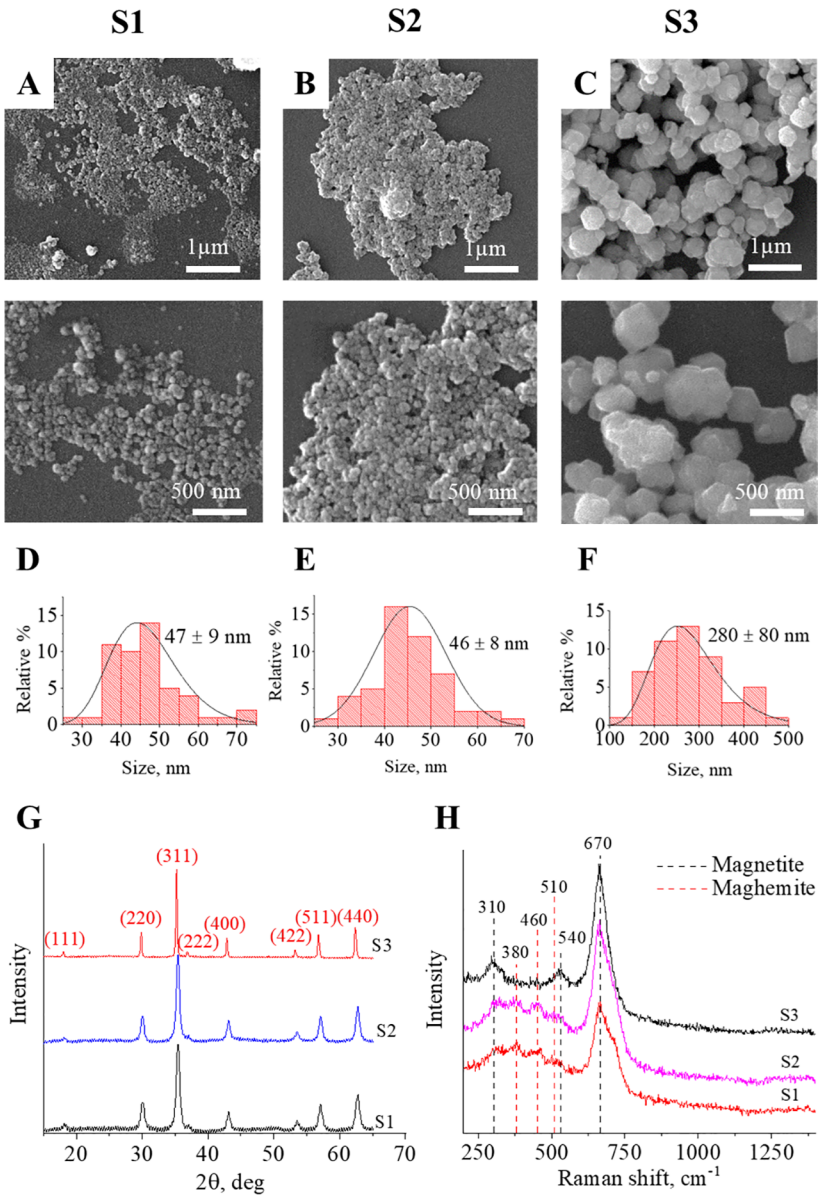

Figure 4. SEM images (A–C), relative size distributions (D–F), XRD patterns (G), and Raman spectra (H) of Fe_3O_4 particles.

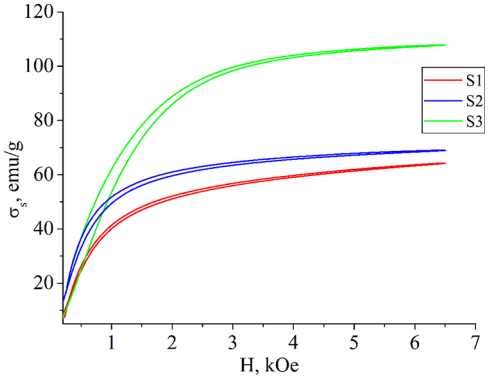

Figure 5. Magnetization curves of the Fe_3O_4 particles produced under various synthesis conditions.

average particle size in the S3 sample compared to S1 and S2. The saturation magnetization of sample S3 is slightly higher than that of polycrystalline magnetite (92–100 emu/g).[29] However, nanoscale powders are found in the literature, which also reveals high saturation magnetization values of more than 100 emu/g.[31] The reason is a para-process occurring in nanosized powders in high magnetic fields and the ordering of magnetic moments in the surface layer of the particles. An important feature of the nanoscale state of magnetite is a higher proportion of atoms belonging to the surface layer relative to the total number of atoms in the particle. Although in macromaterials, the proportion of surface atoms is a fraction of a percentage point of the total amount, in nanoparticles, it can reach 10–60%. Consequently, the influence of the surface layer on the total magnetization of a particle is significantly greater. The surface layer can differ significantly from the interior because the former contains various defects, such as unoccupied nodes, altered coordination of atoms, sites of lattice disorder, and broken exchange bonds. Due to these defects, disordered uncompensated spins emerge. This leads to differences in the resulting magnetization of the surface layer, which noticeably affects the spin configuration of the entire particle. The magnitude of this influence depends on particle

https://doi.org/10.1021/acsabm.2c00496
ACS Appl. Bio Mater. 2022, 5, 3999–4019

Table 2. Crystallite Size, Dislocation Density, Microstress, and Saturation Magnetization of Fe_3O_4 Particles

sample	crystallite size, nm	dislocation density, nm−2	microstress, 10−3	σs (average), emu/g
S1	13 ± 1	6 ± 1	5.8 ± 0.7	64.1 ± 0.1
S2	13 ± 1	6 ± 1	7.0 ± 1.9	69.1 ± 3.7
S3	30 ± 3	2 ± 1	3.8 ± 1.9	107.5 ± 5.1

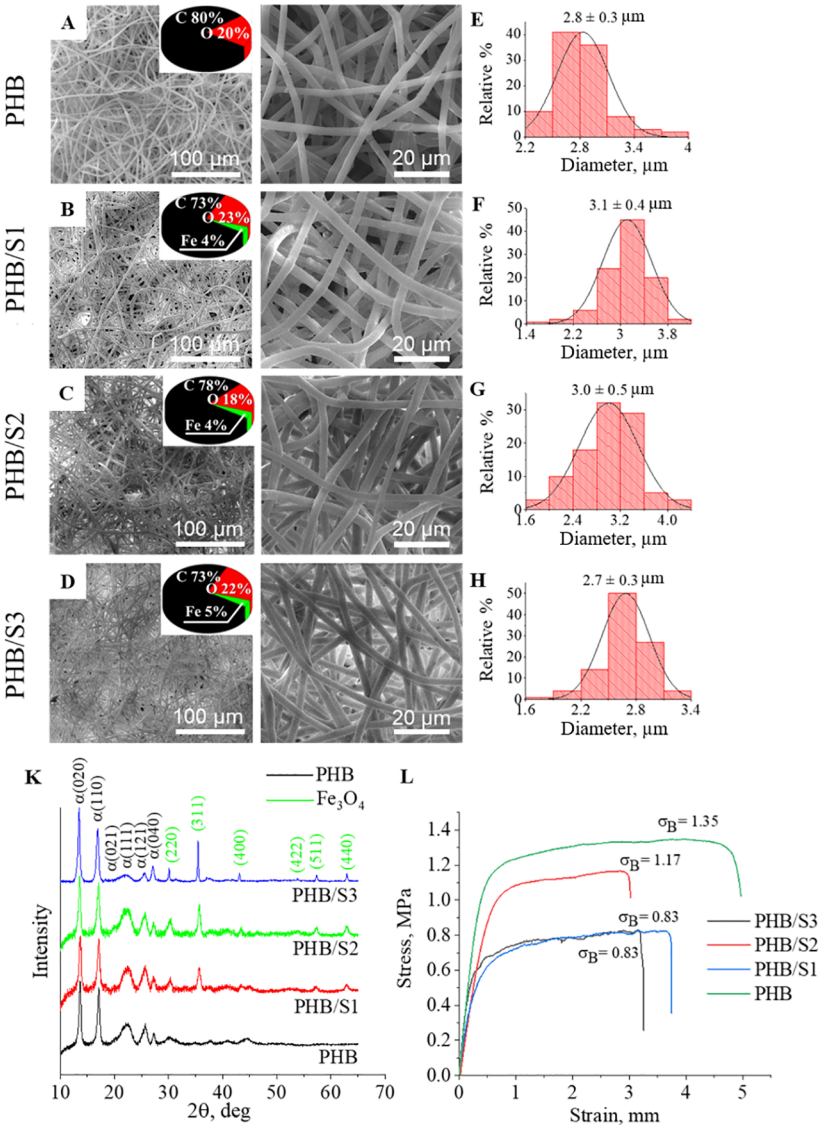

Figure 6. SEM images (A–D), relative fiber diameter distributions (E–H), XRD patterns (K), and tension curves (L) of the composite PHB/Fe_3O_4 scaffolds. Insets illustrate element composition, obtained by energy-dispersive X-ray spectroscopy (analysis), of electrospun composite PHB/Fe_3O_4 fibrous scaffolds.

Table 3. Crystallite Size in Composite PHB/Fe_3O_4 Scaffolds

sample	crystallographic planes of PHB α-phase	crystallite size, nm
PHB	(020)	20
	(110)	15
PHB/S1	(020)	11
	(110)	11
PHB/S2	(020)	11
	(110)	12
PHB/S3	(020)	17
	(110)	17

Table 4. Mechanical Characteristics of Hybrid PHB/Fe_3O_4 Scaffolds after Biodegradation

sample	elongation, %	ultimate strength, MPa	Young's modulus, MPa
PHB	11.0 ± 1.5	1.3 ± 0.1	146 ± 16
PHB/S1	7.6 ± 0.7	0.8 ± 0.2	112 ± 14
PHB/S2	6.8 ± 2.0	1.0 ± 0.2	115 ± 11
PHB/S3	6.3 ± 1.2	0.8 ± 0.1	119 ± 16

size and the thickness of the defective surface layer.[32] Also, defects can be expressed as breaks in the exchange relationships between ions in the tetrahedral positions of the crystal lattice, which leads to the absence of magnetic moments in these positions. It is known that the magnetization from the tetrahedron makes a negative contribution to the final magnetization.[33] Based on the above, we assume that the

https://doi.org/10.1021/acsabm.2c00496
ACS Appl. Bio Mater. 2022, 5, 3999−4019

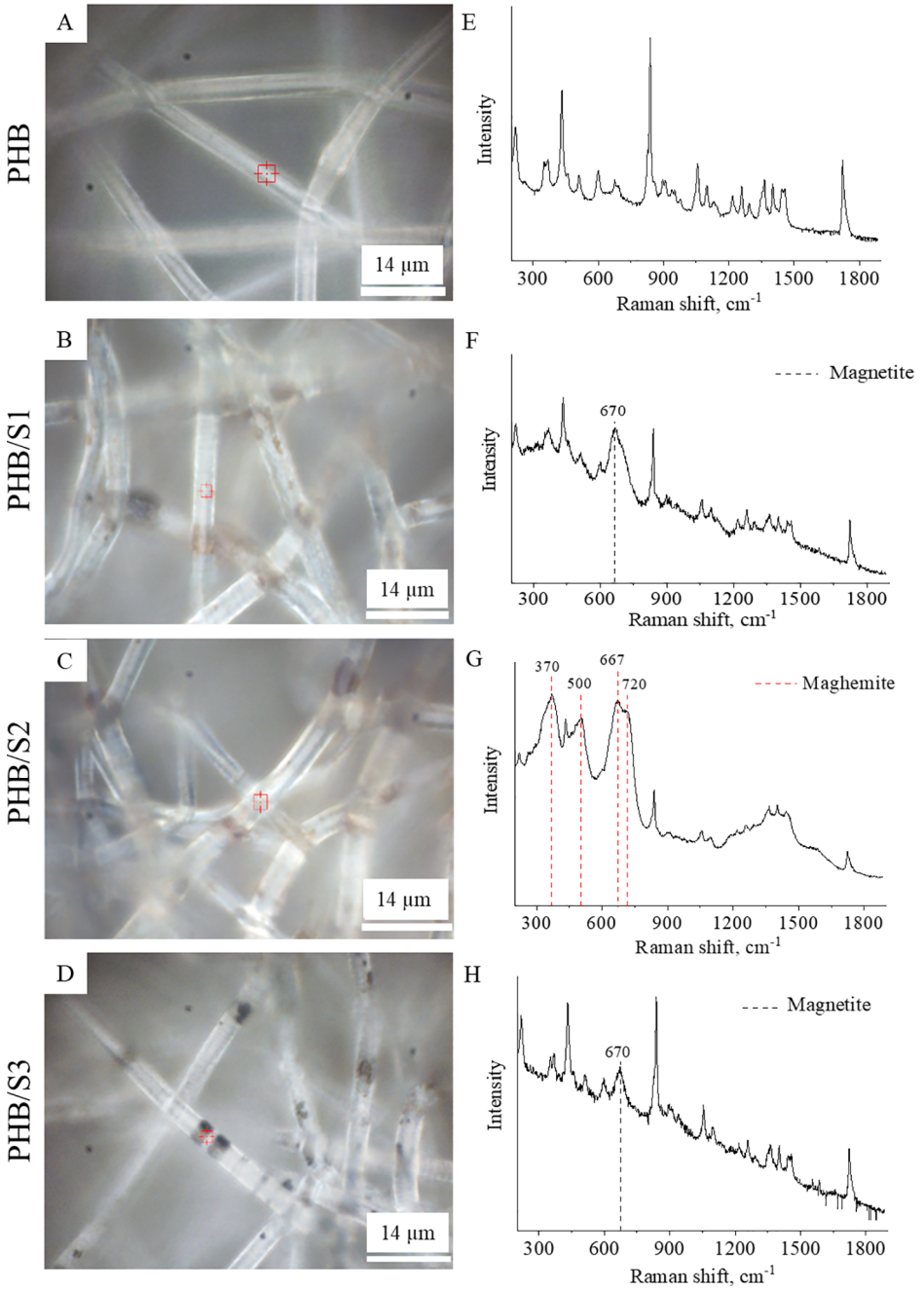

Figure 7. Optical microscopy images (A–D) and Raman spectra (E–H) of the PHB/Fe_3O_4 composite scaffolds.

saturation magnetization may be greater than that of a massive magnetite sample. The crystallite size, dislocation density, microstress, and saturation magnetization of Fe_3O_4 particles are summarized in Table 2.

Thus, two types of magnetite nanoparticles were obtained that have similar size, phase composition, and structure but different surface modifications. It is assumed that CA had an effect on the S1 saturation magnetization values because magnetic nanoparticles are "diluted" with diamagnetic CA. In addition, it is possible that the magnetic characteristics are affected by microstress caused by a high density of dislocations and other lattice defects. The third synthesis route allowed the production of phase-pure MPs of larger size, which have larger values of crystallite size and saturation magnetization. The next step was to study the impact of various MPs on the properties of the electrospun composite scaffolds.

3.2. Characterization of the Electrospun PHB/Fe_3O_4 Composite Scaffolds. The effect of MPs' properties on the morphology of the electrospun fibers was investigated in these experiments. The SEM images (Figure 6A–D) revealed randomly oriented bead-free microfibers with diameters of 2.8 ± 0.3, 3.1 ± 0.4, 3 ± 0.5, and 2.7 ± 0.3 μm for PHB, PHB/S1, PHB/S2, and PHB/S3 scaffolds, respectively.

The diameter distribution of microfibers (Figure 6E–H) revealed no significant differences in the fiber diameter after the addition of MPs of various sizes. The resultant scaffolds contain randomly oriented fibers ensuring interconnected porosity similar to that of the extracellular matrix. The XRD patterns (Figure 6K) of pure PHB and composite PHB/MP

https://doi.org/10.1021/acsabm.2c00496
ACS Appl. Bio Mater. 2022, 5, 3999–4019

Table 5. Raman Shifts and Assignment of the Raman Bands of PHB[38]

Raman shift, cm^{-1}	assignment
1725	C═O stretching vibrations (crystalline phase)
1460	CH_3 asymmetric bending vibrations
1443	CH_2 bending vibrations
1402	CH_3 symmetric bending vibrations
1365	CH bending vibrations and CH_3 symmetric bending vibrations
1295	CH bending vibrations
1261	C−O−C stretching vibrations and CH bending vibrations
1220	C−O−C asymmetric stretching vibrations
1101	C−O−C symmetric stretching vibrations
1058	C−O stretching vibrations
953	C−C stretching vibrations and CH3 rocking bending vibrations
841	C−COO stretching vibrations
691	C═O bending vibrations (in-plane)
680	C═O bending vibrations (out of plane)
598	C−CH_3 and CCO bending vibrations
510	C−CH_3 and CCO bending vibrations
367	C−CH_3 and CCO bending vibrations
351	C−CH_3 and CCO bending vibrations
222	CH_3 torsion bending vibrations

scaffolds contain the main characteristic peaks of the crystalline PHB phase at 13.6° (020) and 16.9° (110). There are also reflections near 22.4° (111), 25.5° (121), 26.9° (040), and 19.9° (021) belonging to planes of the α-phase of PHB (ICDD PDF card no. 00-068-1411). Peaks at 30.37° (220), 35.87

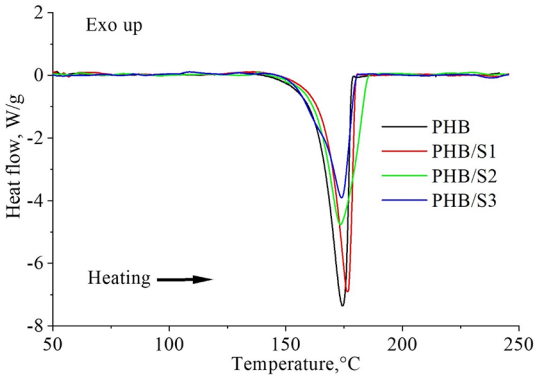

Figure 9. DSC heating curves of the composite PHB/Fe_3O_4 scaffolds.

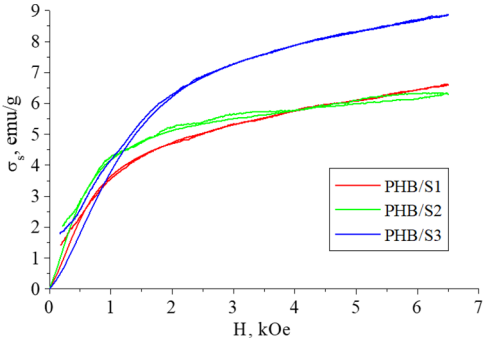

Figure 10. Magnetization curves of the composite PHB/Fe_3O_4 scaffolds.

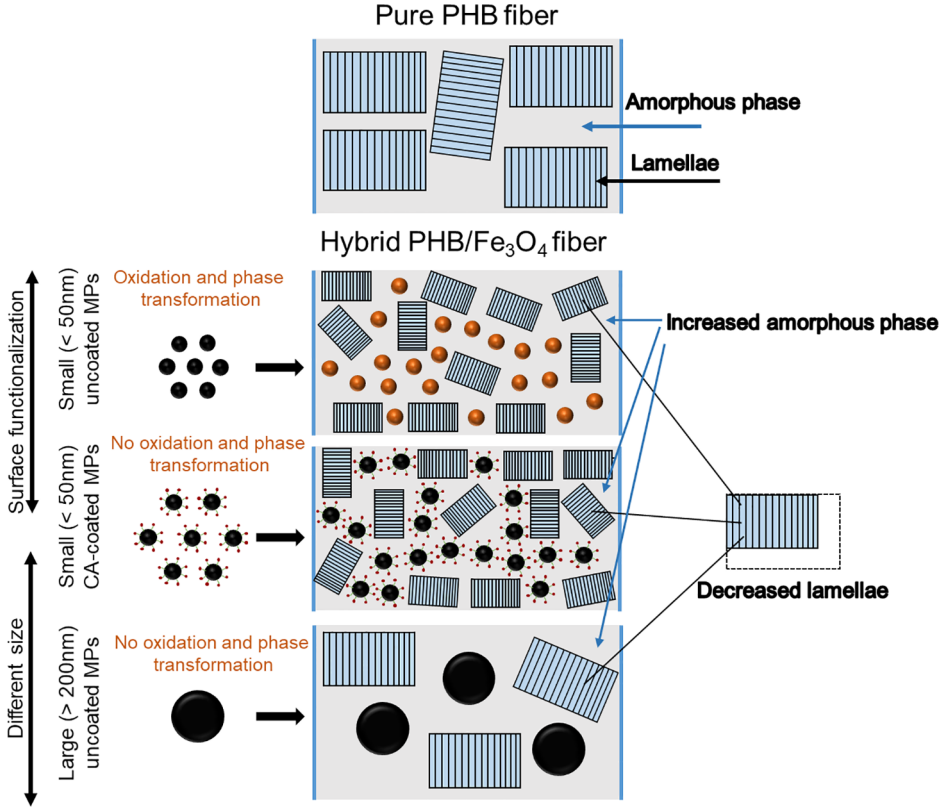

Figure 8. Schematic representation of alterations in the crystalline structure of electrospun PHB fibers as a consequence of the incorporation of MPs as well as phase transformation of MPs proceeding during scaffold fabrication.

https://doi.org/10.1021/acsabm.2c00496
ACS Appl. Bio Mater. 2022, 5, 3999−4019

Table 6. DSC Data and Saturation Magnetization of Pure PHB and Composite PHB/Fe_3O_4 Scaffolds

material	Tm, °C	ΔHm, J/g	Xc,%	$\sigma_{s(average)}$, emu/g
PHB	174.3	82	56	
PHB/S1	176.1	71	48	6.6 ± 0.3
PHB/S2	173.3	77	53	6.3 ± 0.3
PHB/S3	174	55	38	8.8 ± 0.5

(311), 43.53° (400), 53.52° (422), 57.72° (511), and 63.12° (440), corresponding to the magnetite, are also present in the XRD patterns of all composite PHB/Fe_3O_4 scaffolds. In addition, the crystallite size was calculated according to Scherrer's equation. The results, summarized in Table 3, revealed that the crystallite sizes decreased in (020) and (110) directions after MP addition. Therefore, the presence of MPs reduced the mobility of PHB polymer chains, thereby limiting the growth of lamellae.[34]

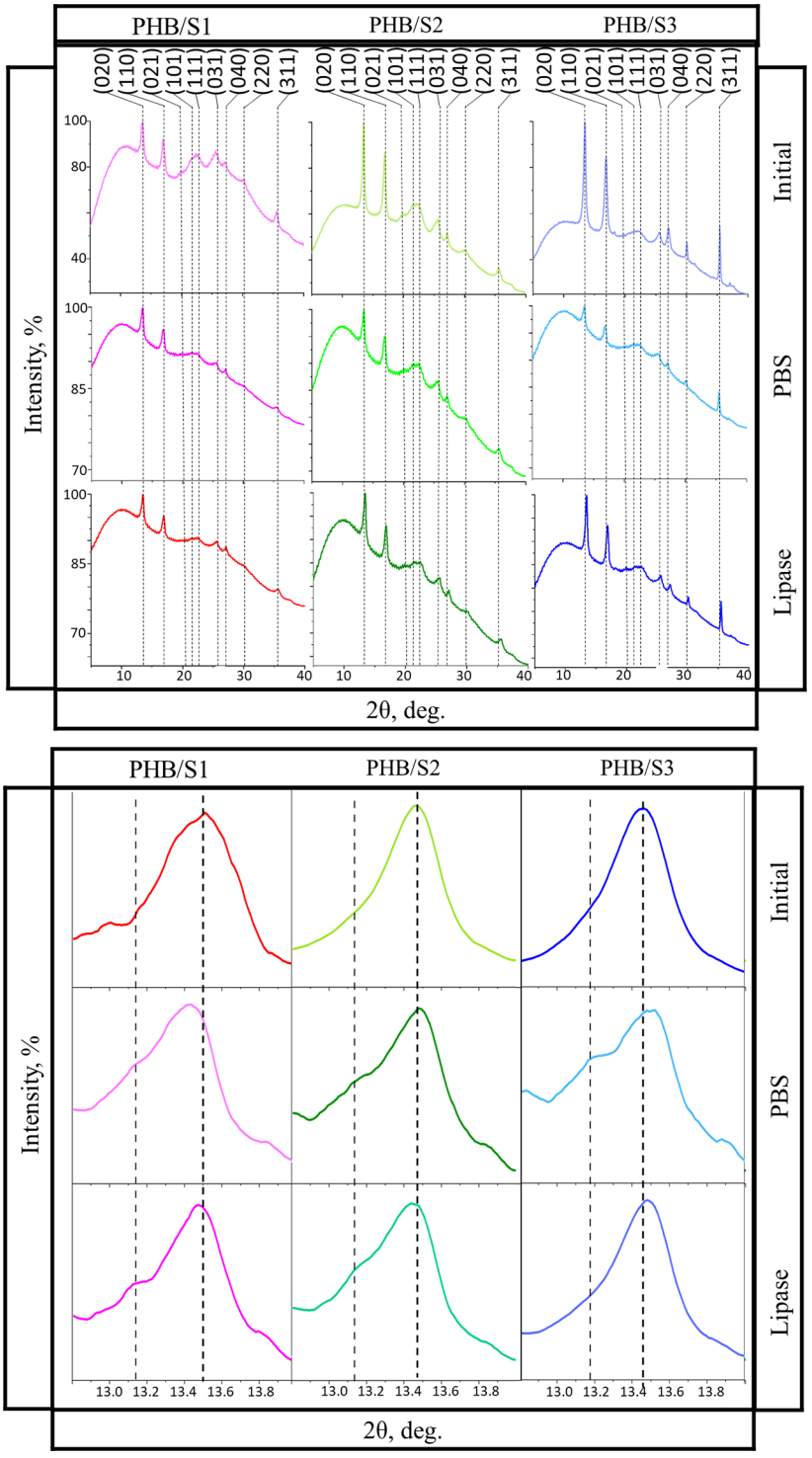

Figure 11. XRD patterns of the hybrid PHB/Fe_3O_4 scaffolds before and after biodegradation in 2θ ranges of (A) 0−40° and (B) 13−14°.

https://doi.org/10.1021/acsabm.2c00496
ACS Appl. Bio Mater. 2022, 5, 3999−4019

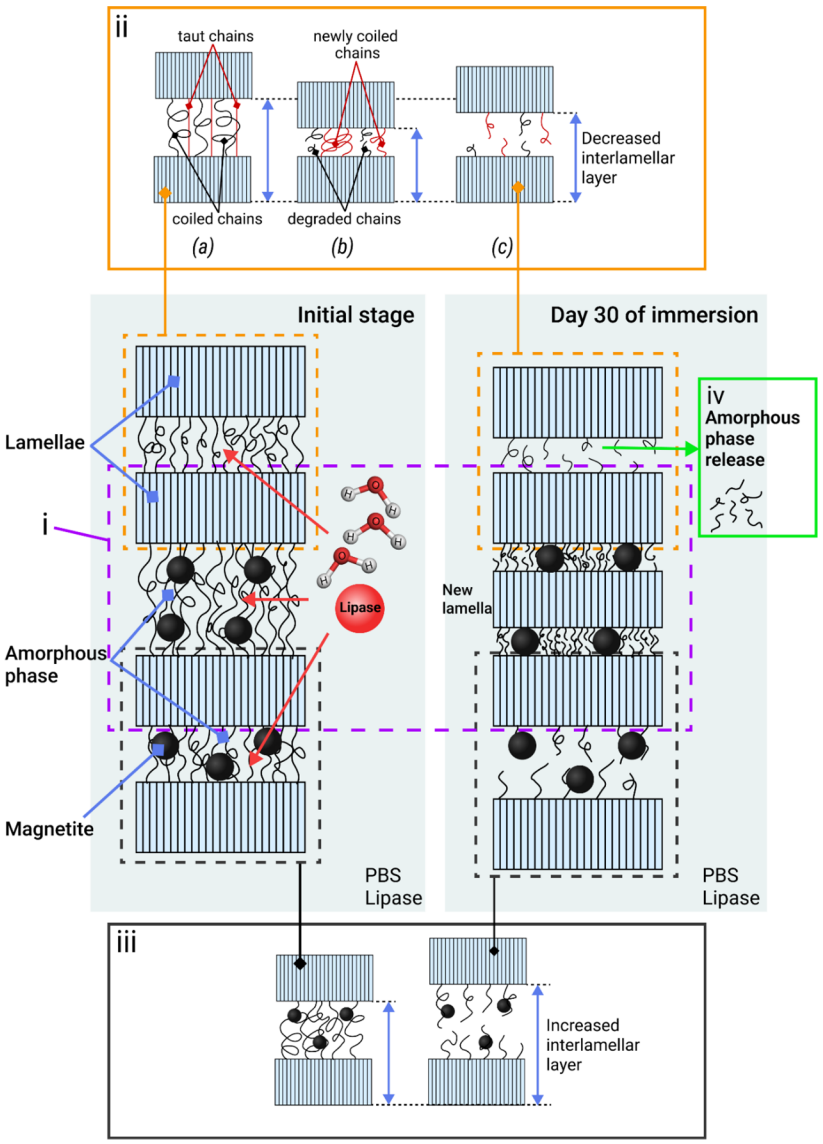

Figure 12. Proposed mechanisms of structural alterations of hybrid PHB/Fe_3O_4 scaffolds during hydrolytic and enzymatic degradation.

The stress−strain curves of the composite PHB/MP scaffolds are shown in Figure 6L. Incorporation of all types of the analyzed MPs slightly lowered ultimate strength, elongation at break, and Young's modulus of the composite PHB/MP scaffolds. Furthermore, the results of tensile tests indicated that the elongation at break is greater in scaffolds containing nanoparticles coated with CA (PHB/S1) than in scaffolds doped with MPs without a surfactant (PHB/S2 and PHB/S3). Homogeneous dispersion of CA-coated particles in the polymer and stronger interaction between these phases (as compared to other PHB/MP composites) improved the mechanical properties, consistently with the results reported in the literature.[35] The investigation of mechanical properties allowed us to determine elongation at break, ultimate strength, and Young's modulus of the studied scaffolds (Table 4).

Deterioration of mechanical characteristics of the composites in comparison with the pure PHB scaffold is due to the agglomeration of MPs. The presence of MPs gave rise to microcracks and reduced polymer chains' mobility, thereby limiting the ability of the polymer chains to transfer emerging stresses to adjacent polymer chains. One of the ways to control the dispersion of particles in a polymer scaffold and to strengthen the bond of MPs with the polymer is the functionalization of the particle surface. For example, in ref 36, Fe_2O_3 nanoparticles were functionalized with a bifunctional binding agent (methacryloxypropyl trimethoxysilane), and better dispersion of nanoparticles and hence greater tensile strength were achieved as compared to nanocomposites based on vinyl ester resins (in the initial state) filled with nanoparticles. Well-dispersed nanoparticles are tightly bound to the polymer matrix owing to the bonding effect between the nanoparticles and the polymer matrix. Consequently, in composites reinforced with functionalized iron oxide nanoparticles, the stress can be more easily transferred from the matrix to the particles, thereby reducing the stress concentration.

Optical microscopy images of the composite microfibrous scaffolds are presented in Figure 7A−D. There are defect-free fibers doped with MPs. It was also revealed that the MPs are inside the fibers and have a brownish color in PHB/S1 and PHB/S2, whereas the MPs in PHB/S3 composites are black. This means that the PHB/MP scaffold fabrication process

https://doi.org/10.1021/acsabm.2c00496
ACS Appl. Bio Mater. 2022, 5, 3999−4019

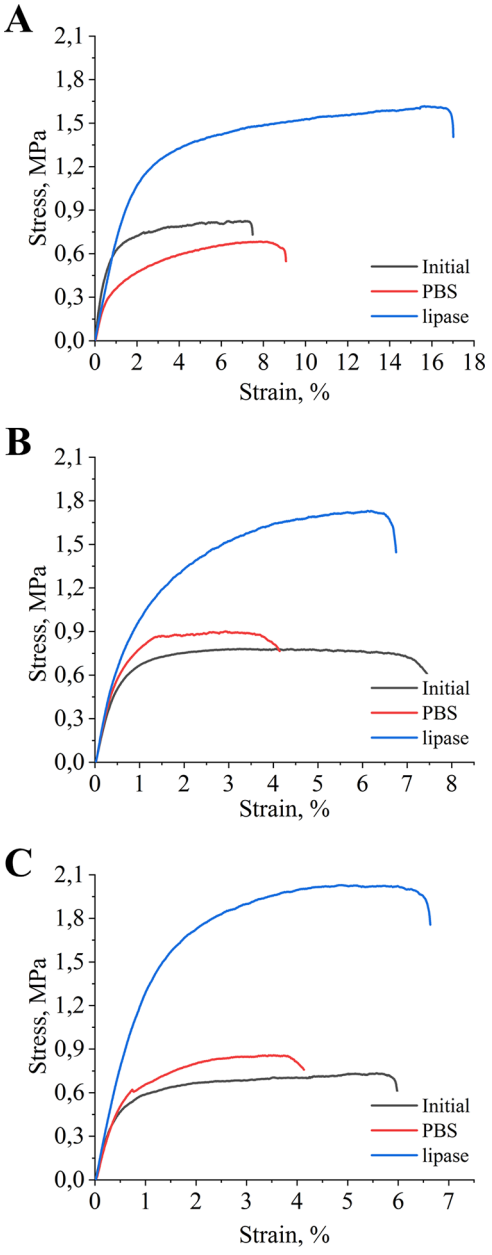

Figure 13. Stress–strain curves of hybrid PHB/S1 (A), PHB/S2 (B), and PHB/S3 (C) scaffolds before and after the biodegradation either in PBS or in the lipase solution.

Table 7. Mechanical Characteristics of Hybrid PHB/Fe_3O_4 Scaffolds after Biodegradation

sample		Young's modulus, MPa	ultimate strength, MPa	elongation, %
PHB/S1	PBS	54 ± 8	0.7 ± 0.2	8.9 ± 3.9
	lipase	70 ± 15	1.5 ± 0.3	17.0 ± 4.8
PHB/S2	PBS	146 ± 21	1.1 ± 0.5	4.5 ± 3.6
	lipase	145 ± 13	1.7 ± 0.1	6.8 ± 0.5
PHB/S3	PBS	119 ± 9	0.9 ± 0.3	4.1 ± 0.7
	lipase	146 ± 14	2.1 ± 0.1	6.6 ± 0.8

gives rise to other forms of iron oxides that are different from magnetite (maghemite).

Raman spectra of pure PHB and composite electrospun scaffolds have been obtained (Figure 7E–H). Raman shifts

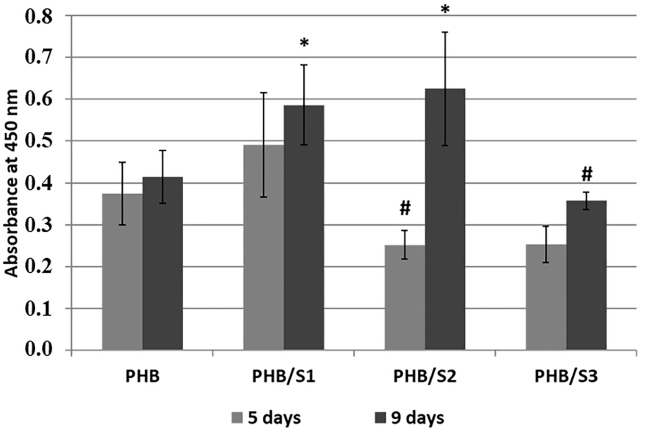

Figure 14. Growth of rMSCs seeded on PHB/Fe_3O_4 composite scaffolds for 5 and 9 days. *p < 0.05 PHB/S1 (ninth day) and PHB/S2 (ninth day) vs PHB (ninth day); #p < 0.05 PHB/S2 (fifth day) and PHB/S3 (fifth day) vs PHB (fifth day).

(cm^{-1}) and assignment of the Raman bands of PHB are summarized in Table 5. For PHB/S1 and PHB/S3 scaffolds (Figure 7F,H), an additional peak at 670 cm^{-1} was noted corresponding to Fe–O symmetric stretching vibrations of magnetite. In the spectrum of the PHB/S2 sample (Figure 7G), there were four additional peaks of maghemite: shifts at 720 and 667 cm^{-1} were assigned to Fe–O symmetric stretching vibrations, and shifts at 500 and 370 cm^{-1} to Fe–O asymmetric bending vibrations. Maghemite forms mainly due to the presence of oxygen in the reaction media of the polymer/MP solution. Unfortunately, the CA coating of S1 nanoparticles could not completely prevent magnetite–maghemite phase transformation. S3 submicron particles showed resistance to the phase transformation during the fabrication of the PHB/S3 scaffolds; this phenomenon can be ascribed to the small surface area of the particles.[37]

Alterations of the crystalline structure of electrospun PHB fibers caused by the incorporation of MPs and phase transformation of MPs occurred during the scaffold fabrication, as schematically depicted in Figure 8. As illustrated there, the sizes of crystalline lamellae of PHB diminished after the incorporation of MPs of all three types into the scaffolds (Table 3). This change is explained by the limited growth of lamellae owing to lowered mobility of polymeric chains restrained by MPs. Therefore, the amorphous phase of hybrid PHB/MP scaffolds is enlarged in comparison with pure PHB fibers. It is important to note that the reduction of lamellae size is most evident in the case of composites doped with nanosized MPs (PHB/S1 and PHB/S2) because of a more homogeneous distribution of MPs within the fiber in comparison with PHB/S3.

Moreover, Raman spectroscopy revealed oxidation and phase transformation (magnetite–maghemite) of unmodified nanosized MPs (S2) during electrospinning owing to the presence of oxygen in the reaction medium. This process was undetectable in case of submicron MPs (S3) because of these particles' smaller surface area, inhibiting their reaction with oxygen. The modification of MPs' surface with CA slightly protected magnetite from oxidation and transformation into maghemite.

Resistance of the particles to the magnetite–maghemite phase transformation is determined by their size, crystal structure, and their functionalization with various surfactants.

https://doi.org/10.1021/acsabm.2c00496
ACS Appl. Bio Mater. 2022, 5, 3999–4019

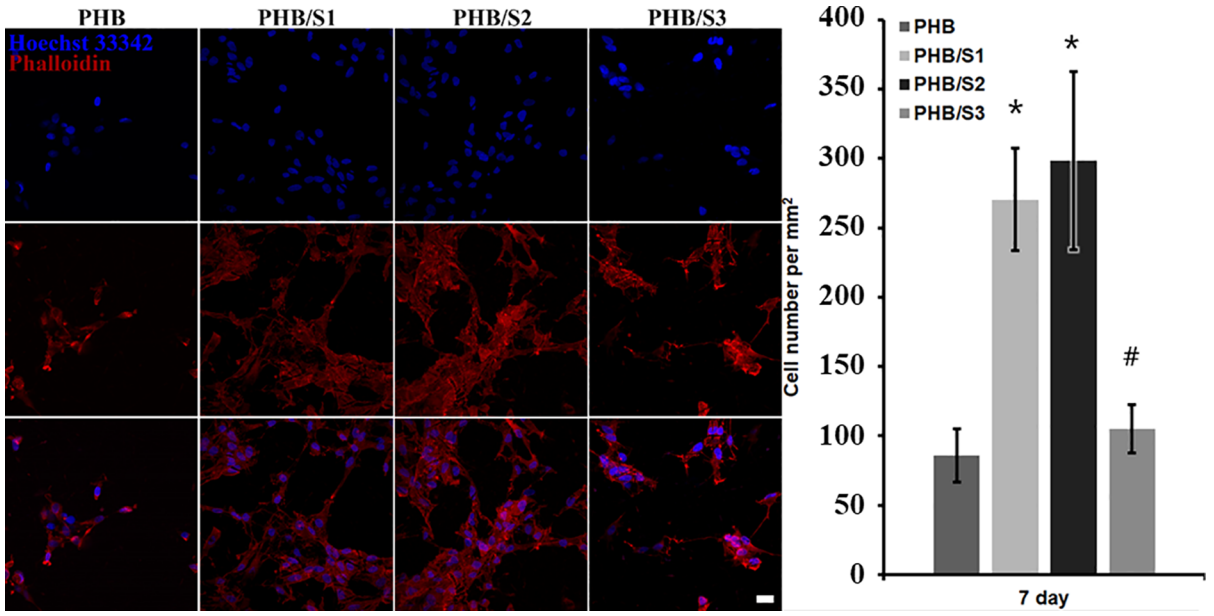

Figure 15. rMSCs seeded on the surface of PHB/Fe_3O_4 composite scaffolds and examined on the seventh day. Confocal images of the cells grown on PHB, PHB/S1, PHB/S2, or PHB/S3 are presented in the left-hand panel. The actin cytoskeleton was visualized using phalloidin-TRITC (red), and nuclei were stained with Hoechst 33342 (blue). Scale bar: 20 μm. In the right-hand panel, quantification data are shown as the mean of the cell number ± SD. *p < 0.05 for PHB/S1 and PHB/S2 vs PHB; #p < 0.05 for PHB/S3 vs PHB/S1 and PHB/S2.

This transformation may arise during the preparation of a solution for electrospinning as a result of ultrasonication of the particles and the concurrent heating and oxidation. Particles of similar sizes (S1 and S2) manifested different resistances to magnetite−maghemite phase transformation due to the formation of the CA layer on the surface of Fe_3O_4 nanoparticles (S1). Thus, uncoated Fe_3O_4 nanoparticles (S2) underwent the strongest oxidation, whereas CA-coated Fe_3O_4 nanoparticles (S1) got oxidized to a lesser extent. Although the coating with CA made it possible to reduce the oxidation state of the particles, it was not feasible to eliminate the phase transformation process. The use of a thicker layer of CA or another surfactant, such as oleic acid, will probably help to obtain phase-pure MPs in a polymer solution. On the other hand, the submicron particles with a more perfect crystal structure (S3) showed resistance to magnetite−maghemite phase transformation.

DSC curves (Figure 9) contained a single melting peak in the range of 173−177 °C. All the scaffolds, except PHB/S1, yielded a relatively sharp melting peak with almost identical melting temperatures (T_m): ∼174 °C.

For PHB/S1 composite scaffolds, T_m was found to be shifted higher, which may be due to the increase in polymer lamellae thickness, consistently with the results reported elsewhere.[39] For PHB/S3 scaffolds, there is a shoulder characterizing multiple melting behaviors of the polymer; this pattern usually contributes either to the melting−recrystallization−remelting process or to the melting of crystals with different lamellar thickness and/or different crystal morphology.[40] Incorporation of MPs decreased the crystallinity of the scaffolds because of the restriction of PHB chains' arrangement after the addition of MPs, in agreement with the results reported before.[20]

Magnetization curves of the composite PHB/Fe_3O_4 scaffolds are shown in Figure 10. The saturation magnetization of the composite PHB/MP electrospun scaffolds turned out to be 6.6 ± 0.3, 6.3 ± 0.3, and 8.8 ± 0.5 emu/g for PHB/S1, PHB/S2, and PHB/S3 samples, respectively. Magnetic PHB/MPs scaffolds obtained in this study possess higher values of magnetization as compared to PHB/MPs composite scaffolds with 11 wt % of MPs (against 8 wt % in our work),[19] which is due to the high values of the saturation magnetization of the magnetite synthesized in this work.

PHB/S3 has the highest saturation magnetization among all the composite scaffolds because S3 submicron particles have the highest saturation magnetization among the analyzed MPs. The phase composition of iron oxide particles in the polymer matrix influenced the saturation magnetization of the electrospun scaffolds. Initially, the nanoparticles coated with CA had the lowest σ_s. Scaffolds doped with uncoated nanoparticles manifested lower saturation magnetization than did the scaffolds doped with CA-coated nanoparticles. The reason is the partial magnetite−maghemite transformation of the nanoparticles, which leads to a decrease in σ_s. The coating of the nanoparticles with CA made it possible to reduce the degree of magnetite−maghemite transformation; accordingly, the σ_s of the scaffolds doped with CA-coated nanoparticles is higher than that of the uncoated ones. Magnetic PHB/MP electrospun scaffolds created in this work have the highest saturation magnetization as compared to PHB/MP composites reported in the literature.[19,20]

Enthalpy (ΔH_m), crystallinity (X_c), and σ_s of the composite PHB/MP scaffolds are presented in Table 6. As mentioned above, MPs of different sizes have dissimilar effects on the structure, crystallinity, and mechanical properties of the PHB polymer scaffolds. MPs affected PHB lamellae growth by reducing the mobility of polymer chains, thereby influencing the structure and crystallinity of the composite scaffolds. The incorporation of submicron MPs (S3) significantly reduced the crystallinity of the hybrid scaffolds but reduced the crystallite size insignificantly as compared with pure PHB scaffolds because MPs interfere with the growth of bigger polymer crystals. For this reason, during the crystallization, small crystallites surrounded by the amorphous phase were found to form. Nanosized Fe_3O_4 particles (S1 and S2) wedged between

https://doi.org/10.1021/acsabm.2c00496
ACS Appl. Bio Mater. 2022, 5, 3999−4019

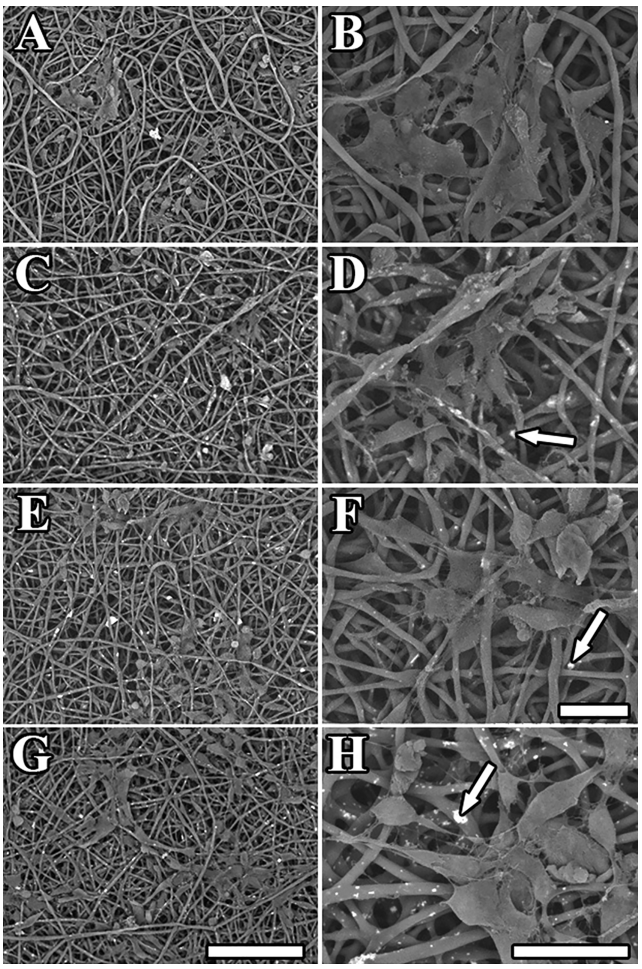

Figure 16. rMSCs seeded on the surface of PHB/Fe_3O_4 composite scaffolds and examined on the seventh day. (A,B) PHB, (C,D) PHB/S1, (E,F) PHB/S2, and (G,H) PHB/S3. SEM, ×500 magnification (A,C,E,G), scale bar: 200 μm. Magnification× 1500 (B,D,F), scale bar: 50 μm; magnification ×2000 (H), scale bar: 30 μm. The white arrows indicate inclusions of magnetite in the fibers of scaffolds.

the lamellae, thereby slightly hindering their crystallization, and we saw the formation of polymer crystals of the same size but smaller than those in pure PHB and PHB/S3 composites.

3.3. Characterization of the Electrospun Composite PHB/Fe_3O_4 Scaffolds after Biodegradation. Mass changes of the PHB/Fe_3O_4 composite scaffolds after degradation in PBS or the lipase solution were investigated by the gravimetric method. For polymers supplemented with unmodified magnetite (PHB/S2 and PHB/S3), no mass changes were detectable after 1 month of incubation in either medium. These findings may be attributed to the negative influence of magnetite on the polymer's biodegradability. In the literature,[41] it has been reported that MPs reduce the scaffold pore size, increase hydrophobicity, and inhibit water absorption, thereby slowing the degradation rate. Additionally, it is known that ferrous (Fe^{2+}) and ferric ions (Fe^{3+}) inhibit pancreatic lipase owing to the destabilization of the enzyme's conformation.[42] Nevertheless, scaffolds with the magnetic nanoparticles modified by CA (PHB/S1) lost 0.3 and 0.2% of the mass in the lipase solution and PBS, respectively. This slight reduction can be explained by the lower hydrophobicity of the modified nanoparticles because of the hydrophilic nature of CA.

To evaluate morphological changes during in vitro biodegradation, SEM analysis of the scaffolds was conducted before and after immersion into hydrolytic and enzymatic media. As displayed in Figure S1 (Supporting Information), no noticeable alterations were observed in any hybrid scaffolds after the incubation in either medium.

Although after the biodegradation, neither a significant mass loss in hybrid scaffolds nor changes in their morphological structure were observed, a reduction in molecular mass of the polymer might still take place. This process has been described in several papers on the biodegradation of polyester materials.[43−45] In general, the molecular mass distribution of polymers shifts toward lower values as a function of immersion time owing to hydrolytic degradation of the ester bonds.[44] Chen et al.[45] have confirmed that during hydrolytic and enzymatic degradation, a molecular weight reduction in a polymeric material occurs earlier than does the weight retention, indicating that the degradation is controlled by diffusion at the initial stage. At this stage, water and lipase molecules diffuse into the amorphous region of the polymer and cause the hydrolysis of the polymer chains. Nonetheless, the decrease in molecular mass does not cause the decrease in the total mass of the scaffolds because the degradation products cannot be desorbed from the polymeric bulk owing to their poor solubility in water and a steric hindrance.[43] To research the influence of biodegradation on the phase composition of MPs in the PHB/Fe_3O_4 composite scaffolds, Raman spectroscopy was performed, and the results are presented in Figure S2 (Supporting Information). For composite scaffolds combined with nanosized MPs (PHB/S1 and PHB/S2), magnetite−maghemite phase transformation was noted. All Raman spectra of the scaffolds with nanosized MPs contain characteristic peaks of the maghemite phase: at 350 cm^{-1} (T_1), 460 cm^{-1} [T_{2g} (2)], 500 cm^{-1} (E), 670 cm^{-1} (A_{1g}), and 720 cm^{-1} (A_1). The band at 670 cm^{-1} (A_{1g}) is related to the symmetrical stretching of oxygen atoms in the FeO_4 tetrahedral group along the [111] direction. Vibrational modes at 500 cm^{-1} (E) and 460 cm^{-1} [T_{2g} (2)] are related to asymmetric bending vibrations of oxygen relative to iron. Vibrational mode A_1 at 720 cm^{-1} was attributed to symmetric stretching vibrations of the Fe−O group. In case of composite scaffolds containing submicron MPs, only three characteristic vibrational modes of the magnetite phase are present: E_g, T_{2g} (3), and A_{1g} at 310, 540, and 670 cm^{-1}, respectively. The vibrational mode E_g at 310 cm^{-1} characterizes the symmetrical shift of oxygen relative to iron, whereas mode T_{2g} (3) arises due to the asymmetric displacement of iron and oxygen, which is due to the displacement of oxygen and iron cations at tetrahedral sites. Thus, submicron MPs proved to be resistant to magnetite−maghemite phase transformation after 30 days of incubation in PBS or the lipase solution.

To study the effect of degradation on the scaffolds' structure, XRD analysis was performed. XRD patterns presented in Figure 11A revealed changes in the intensities of individual lines characteristic of different phases of PHB. Consequently, the biodegradation caused structural changes in the scaffolds. For a more detailed examination of our experimental data, the region of the (020) reflection peak at 13.2° was analyzed. Figure 11B illustrates the changes in shape and position of the (020) reflection of the PHB α-phase after the biodegradation in the tested media.

For the PHB/S1 composite after degradation in either medium and for PHB/S2 after enzymatic degradation, a shift

https://doi.org/10.1021/acsabm.2c00496
ACS Appl. Bio Mater. 2022, 5, 3999−4019

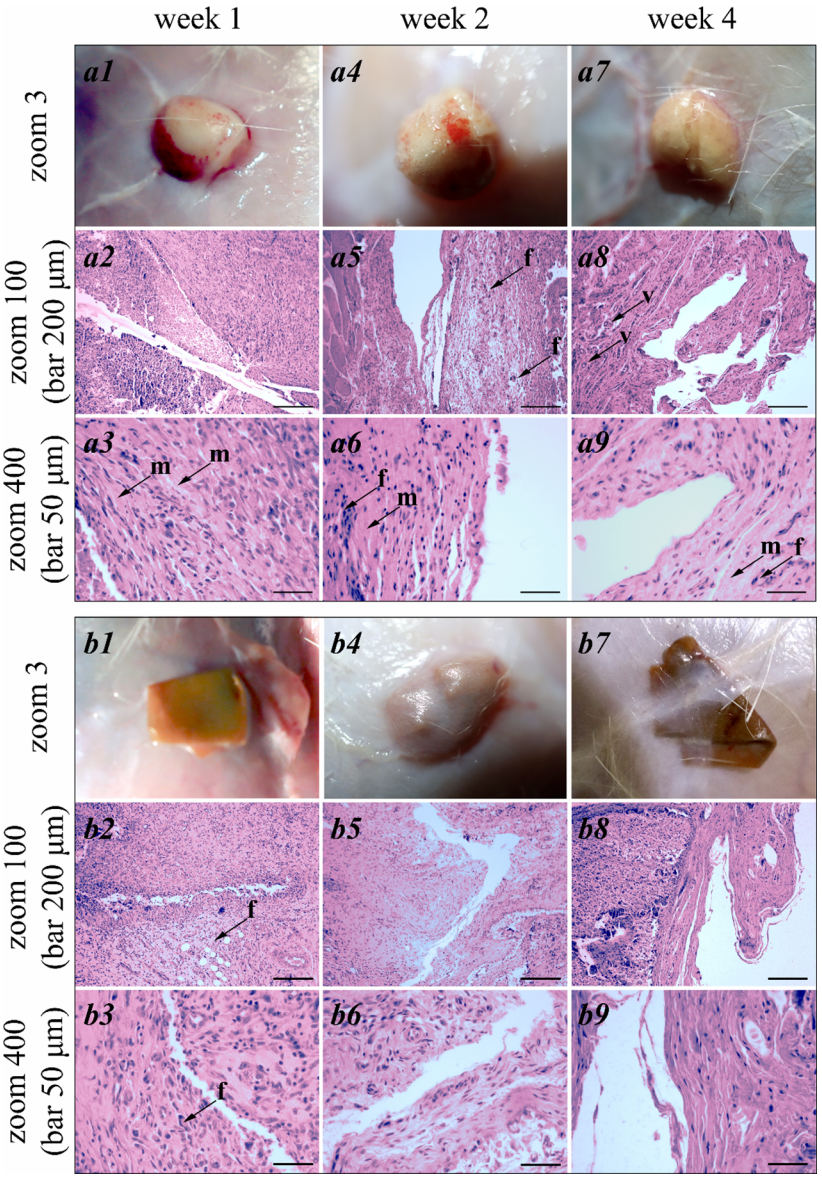

Figure 17. Representative photographs of scaffold implantation sites at low magnification (×3) and hematoxylin−eosin-stained sections at 7 days (a1−a3,b1−b3), 14 days (a4−a6,b4−b6), and 30 days (a7−a9,b7−b9) after subcutaneous implantation of the PHB (a1−a9) and PHB/S1 (b1−b9) scaffolds at high magnification (×100 and ×400). Scale bars represent 50 and 200 μm. Black arrows point to the following: f, FBGCs; m, newly formed extracellular matrix; and v, new blood vessels.

of the (020) reflection toward smaller scattering angles was documented. Moreover, in diffractograms of all the hybrid scaffolds obtained after the degradation, peaks of the (020) plane have a shoulder at 13.2°, which does not match either PHB or Fe_3O_4. This reflection at 13.2° may be considered a splitting of the (020) reflection near 13.6°, implying its partial shift to smaller 2θ angles. These changes in XRD patterns of the composites containing magnetite nanoparticles point to an increase in the polymer's lattice parameters after the degradation, and this increase caused compressive microstresses in the crystalline lamellae.

In contrast, the XRD patterns of hybrid scaffolds containing submicron particles (PHB/S3) represent a shift of (020) reflections toward higher scattering values, indicating a decrease in lattice parameters and hence tensile microstress in polymeric lamellae.

We propose the following mechanism of hydrolytic biodegradation of hybrid PHB/Fe_3O_4 scaffolds, which involves four simultaneous processes, as presented in Figure 12.

It is well known[46−48] that hydrolytic degradation begins in the amorphous phase. Molecules of water and lipase in PBS interact with ester bonds in the amorphous regions, thereby reducing the polymer's molecular mass.[43−45] The cleaved shorter chains possess greater chain mobility,[47] which facilitates the crystallization process in the amorphous phase (Figure 12i). Newly formed lamellae are thinner than the initial ones because they were crystallized from the shorter chains with lower molecular mass.

The polymer's amorphous phase between crystalline lamellae consists of highly coiled and looped and taut chains (Figure 12iia).[46] The conformation of a chain affects its reactivity. Some authors report that highly coiled amorphous chains are more reactive than conformationally strained taut

https://doi.org/10.1021/acsabm.2c00496
ACS Appl. Bio Mater. 2022, 5, 3999−4019

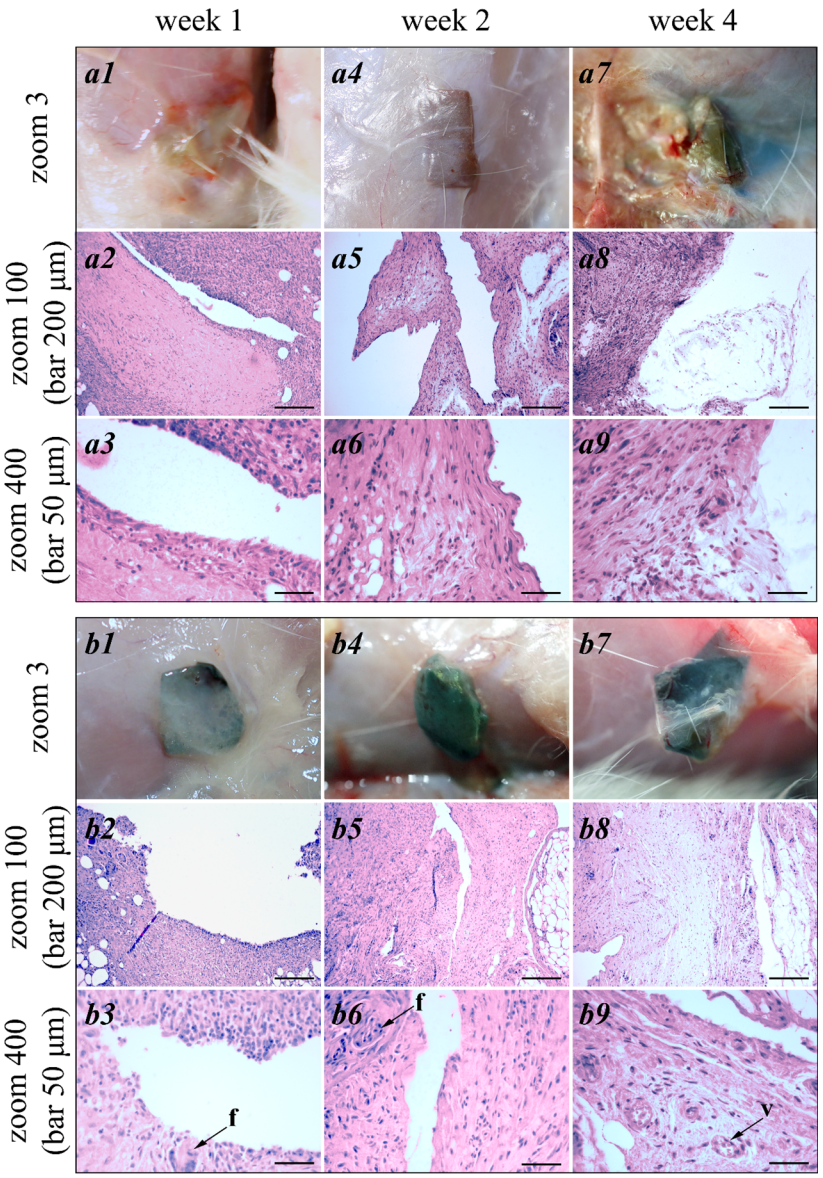

Figure 18. Representative photographs of a scaffold implantation site at low magnification (×3) and hematoxylin−eosin-stained sections at 7 days (a1−a3,b1−b3), 14 days (a4−a6,b4−b6), and 30 days (a7−a9,b7−b9) after subcutaneous implantation of the PHB/S2 (a1−a9) and PHB/S3 (b1−b9) scaffolds at high magnification (×100 and ×400). Scale bars represent 50 and 200 μm. Black arrows indicate the following: f, FBGCs; m, newly formed extracellular matrix; and v, new blood vessels.

ones[49,50] and therefore degrade first. After the breakage of coiled chains, the taut ones can adopt entropically favorable helical conformations (newly coiled chains) and pull the lamellae toward each other, diminishing the interlamellar space (Figure 12iib). Finally, these newly coiled chains undergo biodegradation, and the lamellae connected by them are separated (Figure 12iic). Moreover, according to the XRD data obtained after the degradation, there are tensile microstresses in crystalline lamellae of the PHB/S3 composite; this factor may also contribute to the retention of the interlamellar space.

It is important to note that the mechanism described in Figure 12ii is most evident for the PHB/S3 composite, characterized by the lowest crystallinity (Table 6). Given that MPs are distributed unevenly within the amorphous phase, there are many regions without particles (Figure 8). This mechanism corresponds to the degradation behavior of these particle-free regions.

By contrast, in composites containing nanosized particles (PHB/S1 and PHB/S2), magnetite is distributed more evenly within the amorphous phase (Figure 8). In this case, we suppose the predominance of the process is illustrated in Figure 12iii. After hydrolysis of PHB ester bonds, the interlamellar layer enlarges due to the presence of MPs and compressive microstress revealed by XRD analysis.

It is well known[48] that when amorphous chains in hydrolyzable polymers are broken into shorter ones under biodegradation conditions, oligomeric products are generated that can diffuse out of the polymer bulk and dissolve in the medium (Figure 12iv). Thus, a release of the amorphous phase takes place leaving the polymer more crystalline. According to our gravimetric data, a considerable mass loss did not happen in hybrid scaffolds. Nonetheless, this process most likely takes place, albeit to an extent too small to be detected. Perhaps a

https://doi.org/10.1021/acsabm.2c00496
ACS Appl. Bio Mater. 2022, 5, 3999−4019

degradation period longer than 1 month is needed to register evident mass changes.

To investigate the impact of biodegradation of hybrid scaffolds in either PBS or the lipase solution on their mechanical properties, the mechanical tensile test of scaffolds was carried out after the biodegradation. Stress−strain curves of hybrid PHB/Fe_3O_4 scaffolds before and after the biodegradation in PBS or the lipase solution are shown in Figure 13. The mechanical properties of hybrid PHB/Fe_3O_4 scaffolds are summarized in Table 7.

According to the stress−strain diagrams of hybrid PHB/Fe_3O_4 composite scaffolds obtained either before or after incubation in either PBS or the lipase solution, there was a general increase in ultimate tensile strength. Notably, this parameter went up significantly after the degradation by lipase, whereas the incubation in PBS did not cause such evident alterations. Moreover, in PHB/S2 and PHB/S3, Young's moduli of the scaffolds increased after the biodegradation. Thus, we can conclude that biodegradation improves the stiffness of the material.

A number of papers on the biodegradation of polymers[45,51] and composites[52] point to a decrease of ultimate strength in relation to a significant weight loss in the scaffolds and the decrease in molecular mass. By contrast, after 1 month of the biodegradation in either medium, no mass changes were detectable in the scaffolds. Therefore, the improved stiffness of the scaffolds is a result of the transformation of the amorphous regions into crystalline ones during the degradation.[53] This process has been described by several authors[46,47,54] as cleavage-induced crystallization and is related to the loss of entanglements and tie chains in the amorphous phase, with successive incorporation of these chains into the crystalline regions, increasing their number.

A reduction in elongation at break was observed for PHB/S2 and PHB/S3 composites after the biodegradation in PBS but only for PHB/S2 after the incubation in the lipase solution. Similar results of increased rigidity accompanied by a loss of ductility in the process of degradation have been reported elsewhere.[54] Besides, an unexpected increase of elongation at break was detected in the PHB/S1 composite (after the biodegradation in hydrolytic and enzymatic media) and for PHB/S3 (only after incubation with lipase). Such improved ductility may have several explanations. First, it has been shown that the incorporation of oligomeric chains into a polymer affords a significantly more ductile material.[55] This finding suggests that oligomeric products of biodegradation play the role of a plasticizer by increasing the materials' elongation at break. Because these alterations were more evident during the enzymatic degradation, we can conclude that lipase accelerates chain breakage and oligomer production. Second, several authors have reported that lipase treatment can improve mechanical performance, in particular, the flexibility of different microbial polyesters, through various cross-linking reactions.[56]

Finally, magnetite can affect a polymer's physico−mechanical properties. In the present work, the ultimate strength of PHB composites containing unmodified Fe_3O_4 (PHB/S2 and PHB/S3) improved after biodegradation. On the contrary, the elongation at break declined in PHB/S2 and PHB/S3, and this finding can be attributed to inferior compatibility between PHB and unmodified Fe_3O_4.[57] By contrast, in case of PHB combined with magnetite nanoparticles modified by CA (PHB/S1), simultaneous increases in both ultimate strength and elongation at break were documented, especially after enzymatic degradation. These data can be ascribed to improved interfacial interactions between PHB and Fe_3O_4 owing to their binding via CA molecules and lipase.

3.4. Cell Viability In Vitro. The cell viability assay showed that all the scaffolds can support the growth of rMSCs on their surface; however, cell growth and proliferation were more active on the PHB/S1 and PHB/S2 scaffolds (Figure 14) doped with nanosized MPs. The figure shows the most significant points—the fifth and ninth days of growth. The ability of PHB, PHB/S1, PHB/S2, and PHB/S3 to maintain rMSC growth was also assessed by fluorescence staining with phalloidin and Hoechst 33342 (Figure 15). For cell imaging using microscopy, we have chosen the seventh day of growth, assuming that the number of cells is sufficient and optimal for these methods. On the seventh day of cultivation, a more pronounced increase in cell density was detected on PHB/S1 and PHB/S2, 270.39 ± 19.30 and 298.21 ± 64.17 nuclei per mm^2, respectively. In comparison, on scaffolds PHB and PHB/S3, there were only 85.65 ± 19.30 and 105.09 ± 17.31 nuclei per mm^2.[58]

It was revealed that scaffolds containing submicron MPs (S3) tend to decrease the proliferative activity of rMSCs as compared to the scaffolds doped with nanosized MPs. The cell proliferation on scaffolds PHB/S1 and PHB/S2 was faster than that on PHB scaffolds.

SEM successfully visualized cell growth on various scaffolds (Figure 16A−D). In these images, MPs could be seen as white dots on the fibers. Of note, on the PHB/S1 scaffolds, rMSCs tended to stretch along the fibers, nicely exemplifying contact guidance. On the PHB and PHB/S2 scaffolds, the cells seemed to grow while stretching between scaffold fibers, whereas on PHB/S3 scaffolds, rMSCs also lay on the fibers but tended to form cell clusters including rounded unspread cells.

There are several other factors that can affect cell proliferation, for example, stiffness, surface hydrophilicity, and roughness of scaffold fibers.[59] The mechanical properties of all four types of scaffolds were slightly different from one another (Table 4), whereas the surface topography of separate fibers of the scaffolds could be affected by the difference in the size of the integrated MPs: 46−47 nm (PHB/S1 and PHB/S2) and 280 nm (PHB/S3). In fact, the SEM images of the fibers of the PHB/S3 scaffold uncovered irregular surface topography. For composite PHB/bioactive glass scaffolds, a direct comparison of the effects of particle sizes on bioactivity, biocompatibility, cell proliferation, and protein adsorption has been performed using MG-63 osteoblast-like cells.[60] It was demonstrated that the addition of nanoscale bioactive glass significantly enhances hydrophilicity and protein adsorption of the composite scaffolds by producing a nanotopography promoting cell growth. Jo et al.[61] have also compared the biological performance of hybrid PCL/bioglass micro- and nanocomposites. Nanocomposite scaffolds featured significantly better biocompatibility and osteoblast activity in comparison with the microcomposite scaffolds. Similar results have been reported about the proliferation of mouse embryonic stem cells on nano-, submicro-, and micro-rough surfaces of gold nanoparticle layers: stem cells prefer a surface with a roughness less than 400 nm.[62] hMSCs preferred a roughness of the order of 30 nm compared to 100 nm.[63] Large inclusions of magnetite (with a diameter of ∼3 μm) in the fibers of the PHB/S3 scaffolds are clearly visible in our SEM

https://doi.org/10.1021/acsabm.2c00496
ACS Appl. Bio Mater. 2022, 5, 3999−4019

image (Figure 16H); presumably, this phenomenon may affect cell growth.

3.5. Tissue Reaction to Scaffold Implantation In Vivo.

All the rats used in these experiments survived the surgical procedures without complications such as infection or erosion. On day 7 after the subcutaneous implantation, all the excised samples were characterized by moderate aseptic inflammation with the emergence of a dense fibrous capsule around the scaffolds (Figure 17a1−a3,b1−b3).[64] In all the samples, slight soft-tissue edema was registered at the site of scaffold implantation; this problem arose due to the presence of an exudate in the cavity of the capsules formed around the implants. Microscopic examination on the seventh day revealed that the capsule consisted of a loose connective tissue. In focal inflammation, there is a large amount of a newly formed extracellular matrix, foci of lymphocyte/macrophage infiltration, and foreign body giant cells (FBGCs) were observed (Figures 17a3,b2,b3 and 18b3), which is clearly observed in histological analysis. This can be seen especially well on the seventh day as a large number of cells and their close location at the borders. The overall inflammatory response could be characterized as weak.

On the 14th day of the experiment, the tissue reaction differed among various scaffolds. For the control PHB sample, the edema disappeared with capsule preservation (Figure 17a4−a6), and neoangiogenesis could also be seen on the surface of the capsule, in line with previously reported data.[65] For the PHB/S1 and PHB/S3 scaffolds, the connective-tissue capsule noticeably thickened (Figures 17b4 and 18b4), whereas in the case of the PHB/S1 scaffold, the cell infiltration around the implant disappeared, and vascularization was active in the dense fibrous capsule. 14 days after the implantation of the PHB/S3 scaffold, just as on the seventh day, it continued to show a chronic aseptic inflammatory process around the capsule, expressed in edema, abundant exudation, and an inflammatory infiltrate of leukocytes at the site of sample implantation. Microscopic examination on the 14th day suggested that the capsule consisted of a loose connective tissue and a certain amount of a newly formed extracellular matrix; FBGCs were observed as well (Figures 17a5,b5 and 18a5,b5). The overall inflammatory response could be characterized as weak.

Histological data for day 30 after the implantation indicated identical tissue reactions to all the implanted samples. Aseptic inflammation and edema were not detectable. The fibrous capsules got partially resorbed and acquired a transparent loose appearance (Figures 17a7,b7 and 18a7,b7). Around PHB/S1, PHB/S2, and PHB/S3 scaffolds, aside from a loose capsule, there was active growth of the fibrous tissue throughout the site of implantation of the sample (Figures 17b7 and 18a7,b7), as reported earlier.[66] Besides, an active process of vessel formation (angiogenesis) was in progress at the site of the implanted materials. Microscopic examination on the 30th day showed that the capsule consisted of a loose connective tissue, and there was a certain amount of a newly formed extracellular matrix and a large number of vessels (Figures 17a8 and 18b9); there were FBGCs too. The overall inflammatory response could be characterized as weak.

Based on the results about the tissue reaction after the implantation of the hybrid PHB/Fe_3O_4 scaffolds in Wistar rats, it can be concluded that all the samples in the initial implantation period (7 days) caused mild-to-moderate aseptic inflammation with its subsequent decline at later time points, except for the PHB/S3 sample. The tissue reaction to the PHB/S3 scaffold featured a longer duration of inflammation (days 7 and 14) relative to the other samples. 30 days after the implantation, a loose connective-tissue capsule formed with the general expansion of the fibrous tissue across the entire site of all the studied implants. In accordance with the ISO 10993-6 guidelines, the following scores of the tissue reaction to the implantation of scaffolds were assigned: 1 point for PHB, 1 point for PHB/S1, 1 point for PHB/S2, and 2 points for PHB/S3 (see Appendix E to ISO 10993-6), which defines all scaffolds as having no irritating effect. The excellent biocompatibility of all scaffolds was verified, and they can be recommended for use in tissue engineering, for instance, in the regeneration of nervous tissue, primarily peripheral nerve fibers.

4. CONCLUSIONS

Here, MPs of different sizes and surface chemistry that are spherical and have an average size of 46−280 nm were synthesized by one of the three methods followed by the synthesis of electrospun composite PHB/MP scaffolds. SEM analysis revealed defect-free microfibers with an average diameter of 2.7−3.1 μm. The highest saturation magnetization was documented for submicron MPs synthesized in the presence of ammonia (σ_s = 107.5 ± 5.1 emu/g).

The incorporation of MPs decreased the crystallinity and slightly worsened the mechanical properties of the scaffolds. It was revealed that Fe_3O_4 nanoparticles undergo oxidation and a phase transformation to maghemite during the scaffold fabrication. Composite scaffolds containing nanoparticles manifested better biocompatibility with rMSCs than did pure PHB scaffolds. Submicron MPs showed resistance to magnetite−maghemite phase transformation. After 1 month of incubation in the lipase solution or PBS, scaffolds containing CA-coated MPs lost 0.3 and 0.2% of mass, respectively, whereas no mass changes were seen in other scaffolds. In all the scaffolds, no morphological changes were detected. Scaffolds doped with unmodified MPs possessed greater ultimate strength but smaller elongation at break after the biodegradation. In case of scaffolds combined with CA-coated MPs, immersion into hydrolytic and enzymatic media increased the ultimate strength and elongation at break. Histological assessment of the scaffolds revealed that hybrid PHB/Fe_3O_4 scaffolds promote the formation of blood vessels without a visible inflammatory effect 30 days after implantation. The lowest magnetization was registered for composite PHB/MP scaffolds supplemented with uncoated MPs (6.3 ± 0.3 emu/g) and the highest for composites containing submicron MPs (8.8 ± 0.5 emu/g). Electrospun magnetic PHB/MP scaffolds possess the strongest magnetic properties as compared to PHB/MP composites reported in the literature. Thus, composite PHB scaffolds doped with magnetite nanoparticles coated with CA can be considered the most promising nanomaterial for further studies involving exposure to an external magnetic field because these scaffolds are biocompatible and possess high saturation magnetization.

■ ASSOCIATED CONTENT

Supporting Information

The Supporting Information is available free of charge at https://pubs.acs.org/doi/10.1021/acsabm.2c00496.

https://doi.org/10.1021/acsabm.2c00496
ACS Appl. Bio Mater. 2022, 5, 3999−4019

SEM and optical microscopy images and Raman spectra of the PHB/Fe_3O_4 composite scaffolds before and after 30 days of biodegradation in PBS and lipase (PDF)

AUTHOR INFORMATION

Corresponding Authors

Roman A. Surmenev − *Physical Materials Science and Composite Materials Center, Research School of Chemistry & Applied Biomedical Sciences, National Research Tomsk Polytechnic University, Tomsk 634050, Russia;* orcid.org/0000-0002-8061-3047; Email: rsurmenev@mail.ru

Maria A. Surmeneva − *Physical Materials Science and Composite Materials Center, Research School of Chemistry & Applied Biomedical Sciences, National Research Tomsk Polytechnic University, Tomsk 634050, Russia;* Email: surmenevamaria@mail.ru

Authors

Artyom S. Pryadko A − *Physical Materials Science and Composite Materials Center, Research School of Chemistry & Applied Biomedical Sciences, National Research Tomsk Polytechnic University, Tomsk 634050, Russia*

Yulia R. Mukhortova − *Physical Materials Science and Composite Materials Center, Research School of Chemistry & Applied Biomedical Sciences, National Research Tomsk Polytechnic University, Tomsk 634050, Russia*

Roman V. Chernozem − *Physical Materials Science and Composite Materials Center, Research School of Chemistry & Applied Biomedical Sciences, National Research Tomsk Polytechnic University, Tomsk 634050, Russia*

Igor Pariy − *Physical Materials Science and Composite Materials Center, Research School of Chemistry & Applied Biomedical Sciences, National Research Tomsk Polytechnic University, Tomsk 634050, Russia;* orcid.org/0000-0001-8975-3305

Svetlana I. Alipkina − *Faculty of Biology, M.V. Lomonosov Moscow State University, Moscow 119234, Russia*

Irina I. Zharkova − *Faculty of Biology, M.V. Lomonosov Moscow State University, Moscow 119234, Russia*

Andrey A. Dudun − *Research Center of Biotechnology, Russian Academy of Sciences, Moscow 119071, Russia*

Vsevolod A. Zhuikov − *Research Center of Biotechnology, Russian Academy of Sciences, Moscow 119071, Russia*

Anastasia M. Moisenovich − *Faculty of Biology, M.V. Lomonosov Moscow State University, Moscow 119234, Russia*

Garina A. Bonartseva − *Research Center of Biotechnology, Russian Academy of Sciences, Moscow 119071, Russia*

Vera V. Voinova − *Faculty of Biology, M.V. Lomonosov Moscow State University, Moscow 119234, Russia*

Dariana V. Chesnokova − *Faculty of Biology, M.V. Lomonosov Moscow State University, Moscow 119234, Russia;* orcid.org/0000-0003-1148-7988

Alexey A. Ivanov − *Physical Materials Science and Composite Materials Center, Research School of Chemistry & Applied Biomedical Sciences, National Research Tomsk Polytechnic University, Tomsk 634050, Russia*

Daria Yu. Travnikova − *Faculty of Biology, M.V. Lomonosov Moscow State University, Moscow 119234, Russia*

Konstantin V. Shaitan − *Faculty of Biology, M.V. Lomonosov Moscow State University, Moscow 119234, Russia*

Anton P. Bonartsev − *Faculty of Biology, M.V. Lomonosov Moscow State University, Moscow 119234, Russia*

Dmitry V. Wagner − *National Research Tomsk State University, Tomsk 634050, Russia*

Lada E. Shlapakova − *Physical Materials Science and Composite Materials Center, Research School of Chemistry & Applied Biomedical Sciences, National Research Tomsk Polytechnic University, Tomsk 634050, Russia*

Complete contact information is available at: https://pubs.acs.org/10.1021/acsabm.2c00496

Notes

The authors declare no competing financial interest.

ACKNOWLEDGMENTS

The authors are thankful to S. Sinyavskiy and E. Karpenko (Tomsk Polytechnic University) for the optimization of the nanomaterials' synthesis parameters. The research was carried out at Tomsk Polytechnic University within the framework of the Tomsk Polytechnic University Development Program. Financial support for the magnetization assay from the Ministry of Science and Higher Education is acknowledged (project # 075-15-2021-588 of 1 June 2021). The purchase of materials; the SEM, DSC, and Raman analyses; and the investigation of magnetic properties of the prepared materials were financially supported by the Russian Science Foundation (project # 20-63-47096). The work was done using the equipment located at the User Facilities Center of Moscow State University, including the equipment purchased on account of the MSU Program of Development until 2020. Electron microscopy of rMSCs on scaffolds was performed using the unique equipment setup "3D-EMS" of Moscow State University.

REFERENCES

(1) Hao, L.; Li, L.; Wang, P.; Wang, Z.; Shi, X.; Guo, M.; Zhang, P. Synergistic osteogenesis promoted by magnetically actuated nano-mechanical stimuli. *Nanoscale* **2019**, *11*, 23423−23437.

(2) Russo, T.; Peluso, V.; Gloria, A.; Oliviero, O.; Rinaldi, L.; Improta, G.; De Santis, R.; D'Antò, V. Combination design of time-dependent magnetic field and magnetic nanocomposites to guide cell behavior. *Nanomaterials* **2020**, *10*, 577.

(3) Adedoyin, A. A.; Ekenseair, A. K. Biomedical applications of magneto-responsive scaffolds. *Nano Res.* **2018**, *11*, 5049−5064.

(4) Soares, P. I.; Romão, J.; Matos, R.; Silva, J. C.; Borges, J. P. Design and engineering of magneto-responsive devices for cancer theranostics: Nano to macro perspective. *Prog. Mater. Sci.* **2021**, *116*, 100742.

(5) Cardoso, V. F.; Francesko, A.; Ribeiro, C.; Bañobre-López, M.; Martins, P.; Lanceros-Mendez, S. Advances in magnetic nanoparticles for biomedical applications. *Adv. Healthcare Mater.* **2018**, *7*, 1700845.

(6) Dadfar, S. M.; Roemhild, K.; Drude, N. I.; von Stillfried, S.; Knüchel, R.; Kiessling, F.; Lammers, T. Iron oxide nanoparticles: Diagnostic, therapeutic and theranostic applications. *Adv. Drug Delivery Rev.* **2019**, *138*, 302−325.

(7) Cornell, R. M.; Schwertmann, U. *The Iron Oxides: Structure, Properties, Reactions, Occurrences and Uses*; John Wiley & Sons, 2003.

(8) de Sousa, M. E.; Fernández van Raap, M. B.; Rivas, P. C.; Mendoza Zélis, P.; Girardin, P.; Pasquevich, G. A.; Alessandrini, J. L.; Muraca, D.; Sánchez, F. H. Stability and relaxation mechanisms of citric acid coated magnetite nanoparticles for magnetic hyperthermia. *J. Phys. Chem. C* **2013**, *117*, 5436−5445.

(9) Liu, J.; Dai, C.; Hu, Y. Aqueous aggregation behavior of citric acid coated magnetite nanoparticles: effects of pH, cations, anions, and humic acid. *Environ. Res.* **2018**, *161*, 49−60.

(10) Li, L.; Mak, K.; Leung, C. W.; Chan, K.; Chan, W.; Zhong, W.; Pong, P. Effect of synthesis conditions on the properties of citric-acid

coated iron oxide nanoparticles. *Microelectron. Eng.* **2013**, *110*, 329−334.
(11) Niiyama, E.; Uto, K.; Lee, C. M.; Sakura, K.; Ebara, M. Alternating magnetic field-triggered switchable nanofiber mesh for cancer thermo-chemotherapy. *Polymers* **2018**, *10*, 1018.
(12) Bock, N.; Riminucci, A.; Dionigi, C.; Russo, A.; Tampieri, A.; Landi, E.; Goranov, V. A.; Marcacci, M.; Dediu, V. A novel route in bone tissue engineering: magnetic biomimetic scaffolds. *Acta Biomater.* **2010**, *6*, 786−796.
(13) Kim, J.-J.; Singh, R. K.; Seo, S.-J.; Kim, T.-H.; Kim, J.-H.; Lee, E.-J.; Kim, H.-W. Magnetic scaffolds of polycaprolactone with functionalized magnetite nanoparticles: physicochemical, mechanical, and biological properties effective for bone regeneration. *RSC Adv.* **2014**, *4*, 17325−17336.
(14) Ge, J.; Zhai, M.; Zhang, Y.; Bian, J.; Wu, J. Biocompatible Fe_3O_4 / chitosan scaffolds with high magnetism. *Int. J. Biol. Macromol.* **2019**, *128*, 406−413.
(15) Barhoum, A.; Pal, K.; Rahier, H.; Uludag, H.; Kim, I. S.; Bechelany, M. Nanofibers as new-generation materials: from spinning and nano-spinning fabrication techniques to emerging applications. *Appl. Mater. Today* **2019**, *17*, 1−35.
(16) Khorshidi, S.; Solouk, A.; Mirzadeh, H.; Mazinani, S.; Lagaron, J. M.; Sharifi, S.; Ramakrishna, S. A review of key challenges of electrospun scaffolds for tissue-engineering applications. *J. Tissue Eng. Regener. Med.* **2016**, *10*, 715−738.
(17) Grigore, M. E.; Grigorescu, R. M.; Iancu, L.; Ion, R.-M.; Zaharia, C.; Andrei, E. R. Methods of synthesis, properties and biomedical applications of polyhydroxyalkanoates: a review. *J. Biomater. Sci., Polym. Ed.* **2019**, *30*, 695−712.
(18) Goonoo, N.; Bhaw-Luximon, A.; Passanha, P.; Esteves, S. R.; Jhurry, D. Third generation poly (hydroxyacid) composite scaffolds for tissue engineering. *J. Biomed. Mater. Res., Part B* **2017**, *105*, 1667−1684.
(19) Sangsanoh, P.; Supaphol, P. Poly (3-hydroxybutyrate)/ magnetite composite nanofibers obtained via combined electrospinning and ammonia gas-enhancing in situ co-precipitation: Preparation and potential use in biomedical applications. *Chiang Mai J. Sci.* **2014**, *41*, 676−690.
(20) Ho, M. H.; Li, S. Y.; Ciou, C. Y.; Wu, T. M. The morphology and degradation behavior of electrospun poly(3-hydroxybutyrate)/ Magnetite and poly(3-hydroxybutyrate-co-3-hydroxyvalerate)/Magnetite composites. *J. Appl. Polym. Sci.* **2014**, *131*, 41070.
(21) Sajjad, S.; Leghari, S. A. K.; Jabeen, N.; Riaz, N.; Tariq, M.; Ahmed, I.; Maaza, M. Fe_3O_4 nanorods r-GO sheets nanocomposite visible photo catalyst. *Mater. Res. Express* **2019**, *6*, 065013.
(22) Cullity, B. D. *Elements of X-ray Diffraction*; Addison-Wesley Publishing, 1956.
(23) Chen, L.; Wang, M. Production and evaluation of biodegradable composites based on PHB−PHV copolymer. *Biomaterials* **2002**, *23*, 2631−2639.
(24) Kreslin, V. Y.; Naiden, E. Automatic complex for a study of the characteristics of hard magnetic materials. *Instrum. Exp. Tech.* **2002**, *45*, 55−57.
(25) Zhuikov, V.; Bonartsev, A.; Makhina, T.; Myshkina, V.; Voinova, V.; Bonartseva, G.; Shaitan, K. Hydrolytic Degradation of Poly (3-Hydroxybutyrate) and Its Copolymer with 3-Hydroxyvalerate of Different Molecular Weights in vitro. *Biophys* **2018**, *63*, 169−176.
(26) Bonartsev, A.; Zharkova, I.; Voinova, V.; Kuznetsova, E.; Zhuikov, V.; Makhina, T.; Myshkina, V.; Potashnikova, D.; Chesnokova, D.; Khaydapova, D. Poly (3-hydroxybutyrate)/poly (ethylene glycol) scaffolds with different microstructure: the effect on growth of mesenchymal stem cells. *3 Biotech* **2018**, *8*, 1−10.
(27) Froes, B.; Holgado, L. A.; Simões, R. D.; Velasco Nieto, D.; Angel Rodriguez Perez, M.; Kinoshita, A. Tissue reaction after subcutaneous implants of a new material composed of ethylene-vinyl acetate and starch for future use as a biomaterial. *J. Biomed. Mater. Res., Part B* **2019**, *107*, 400−407.
(28) Wang, X.; Zhao, Z.; Qu, J.; Wang, Z.; Qiu, J. Fabrication and characterization of magnetic Fe_3O_4−CNT composites. *J. Phys. Chem. Solids* **2010**, *71*, 673−676.
(29) Araújo, A.; Rodrigues, A.; Azevedo, W.; Machado, F.; Rezende, S. Sustained magnetization oscillations in polyaniline-Fe_3O_4 nanocomposites. *J. Chem. Phys.* **2015**, *143*, 124706.
(30) Liu, Q.; Xu, Z. Functionalization and applications of nanosized γ-Fe_2O_3 particles. *J. Appl. Phys.* **1996**, *79*, 4702−4704.
(31) Hou, Y.; Yu, J.; Gao, S. Solvothermal reduction synthesis and characterization of superparamagnetic magnetite nanoparticles. *J. Mater. Chem.* **2003**, *13*, 1983−1987.
(32) Naiden, E.; Rodionov, V. Analysis of the ground state of a nanosized ferrimagnetic particle. *Russ. Phys. J.* **2012**, *55*, 394−399.
(33) Sitidze, Y.; Sato, H. *Ferrites [Russian translation]*; Mir, 1964.
(34) Phongtamrug, S.; Tashiro, K. X-ray Crystal Structure Analysis of Poly (3-hydroxybutyrate) β-Form and the Proposition of a Mechanism of the Stress-Induced α-to-β Phase Transition. *Macromolecules* **2019**, *52*, 2995−3009.
(35) Liu, H.; Webster, T. J. Mechanical properties of dispersed ceramic nanoparticles in polymer composites for orthopedic applications. *Int. J. Nanomed.* **2010**, *5*, 299.
(36) Guo, Z.; Lei, K.; Li, Y.; Ng, H. W.; Prikhodko, S.; Hahn, H. T. Fabrication and characterization of iron oxide nanoparticles reinforced vinyl-ester resin nanocomposites. *Compos. Sci. Technol.* **2008**, *68*, 1513−1520.
(37) Khan, U. S.; Manan, A.; Khan, N.; Mahmood, A.; Rahim, A. Transformation mechanism of magnetite nanoparticles. *Mater. Sci.-Pol.* **2015**, *33*, 278−285.
(38) Furukawa, T.; Sato, H.; Murakami, R.; Zhang, J.; Noda, I.; Ochiai, S.; Ozaki, Y. Raman microspectroscopy study of structure, dispersibility, and crystallinity of poly (hydroxybutyrate)/poly (l-lactic acid) blends. *Polymer* **2006**, *47*, 3132−3140.
(39) Gunaratne, L. W. K.; Shanks, R. Miscibility, melting, and crystallization behavior of poly (hydroxybutyrate) and poly (D, L-lactic acid) blends. *Polym. Eng. Sci.* **2008**, *48*, 1683−1692.
(40) Gunaratne, L.; Shanks, R. Melting and thermal history of poly (hydroxybutyrate-co-hydroxyvalerate) using step-scan DSC. *Thermochim. Acta* **2005**, *430*, 183−190.
(41) Ghorbani, F.; Zamanian, A.; Shams, A.; Shamoosi, A.; Aidun, A. Fabrication and characterisation of super-paramagnetic responsive PLGA-gelatine-magnetite scaffolds with the unidirectional porous structure: a physicochemical, mechanical, and in vitro evaluation. *IET Nanobiotechnol.* **2019**, *13*, 860−867.
(42) Dong, H.; Gao, S.; Han, S.-p.; Cao, S.-g. Purification and characterization of a Pseudomonas sp. lipase and its properties in non-aqueous media. *Biotechnol. Appl. Biochem.* **1999**, *30*, 251−256.
(43) Boskhomdzhiev, A. P.; Bonartsev, A. P.; Makhina, T. K.; Myshkina, V. L.; Ivanov, E. A.; Bagrov, D. V.; Filatova, E. V.; Iordanskii, A. L.; Bonartseva, G. A. Biodegradation kinetics of poly(3-hydroxybutyrate)-based biopolymer systems. *Biochem. (Mosc.) Suppl. B: Biomed. Chem.* **2010**, *4*, 177−183.
(44) Gil-Castell, O.; Badia, J. D.; Bou, J.; Ribes-Greus, A. Performance of Polyester-Based Electrospun Scaffolds under In Vitro Hydrolytic Conditions: From Short-Term to Long-Term Applications. *Nanomaterials* **2019**, *9*, 786.
(45) Chen, X. Y.; Yang, X. D.; Pan, J. Y.; Wang, L.; Xu, K. T. Degradation Behaviors of Bioabsorbable P3/4HB Monofilament Suture In Vitro and In Vivo. *J. Biomed. Mater. Res., Part B* **2010**, *92B*, 447−455.
(46) King, E.; Cameron, R. E. Effect of hydrolytic degradation on the microstructure of poly(glycolic acid): An X-ray scattering and ultraviolet spectrophotometry study of wet samples ultraviolet. *J. Appl. Polym. Sci.* **1997**, *66*, 1681−1690.
(47) Zong, X. H.; Wang, Z. G.; Hsiao, B. S.; Chu, B.; Zhou, J. J.; Jamiolkowski, D. D.; Muse, E.; Dormier, E. Structure and morphology changes in absorbable poly(glycolide) and poly(glycolide-co-lactide) during in vitro degradation. *Macromolecules* **1999**, *32*, 8107−8114.
(48) Zhuikov, V. A.; Bonartsev, A. P.; Bagrov, D. V.; Yakovlev, S. G.; Myshkina, V. L.; Makhina, T. K.; Bessonov, I. V.; Kopitsyna, M. N.;

https://doi.org/10.1021/acsabm.2c00496
ACS Appl. Bio Mater. 2022, 5, 3999−4019

Morozov, A. S.; Rusakov, A. A.; Useinov, A. S.; Shaitan, K. V.; Bonartseva, G. A. Mechanics and surface ultrastructure changes of poly(3-hydroxybutyrate) films during enzymatic degradation in pancreatic lipase solution. *Mol. Cryst. Liq. Cryst.* **2017**, *648*, 236−243.
(49) Shibryaeva, L. S.; Kiryushkin, S. G.; Zaikov, G. E. Autooxidation of Oriented Polyolefins. *Polym. Degrad. Stab.* **1992**, *16*, 71−93.
(50) Rapoport, N. Y.; Goniashvili, A. S.; Akutin, M. S.; Miller, V. B. *Features of Low-Temperature Oxidation of Oriented Polypropylene Initiated by γ-radiolysis*; Vysokomolekulyarnye Soedineniya. Seriya A, 1977; pp 2211−2216.
(51) Ferreira, J.; Gloria, A.; Cometa, S.; Coelho, J. F. J.; Domingos, M. Effect of in vitro enzymatic degradation on 3D printed poly(epsilon-caprolactone) scaffolds: morphological, chemical and mechanical properties. *J. Appl. Biomater. Funct. Mater.* **2017**, *15*, E185−E195.
(52) Heidari, F.; Razavi, M.; Bahrololoom, M. E.; Yazdimamaghani, M.; Tahriri, M.; Kotturi, H.; Tayebi, L. Evaluation of the mechanical properties, in vitro biodegradability and cytocompatibility of natural chitosan/hydroxyapatite/nano-Fe_3O_4 composite. *Ceram. Int.* **2018**, *44*, 275−281.
(53) Løvdal, A.; Vange, J.; Nielsen, L. F.; Almdal, K. Mechanical properties of electrospun PCL scaffold under in vitro and accelerated degradation conditions. *Biomed. Eng. - Appl. Basis Commun.* **2014**, *26*, 1450043.
(54) Lovera, D.; Marquez, L.; Balsamo, V.; Taddei, A.; Castelli, C.; Muller, A. J. Crystallization, morphology, and enzymatic degradation of polyhydroxybutyrate/polycaprolactone (PHB/PCL) blends. *Macromol. Chem. Phys.* **2007**, *208*, 924−937.
(55) Burgos, N.; Tolaguera, D.; Fiori, S.; Jimenez, A. Synthesis and Characterization of Lactic Acid Oligomers: Evaluation of Performance as Poly(Lactic Acid) Plasticizers. *J. Polym. Environ.* **2014**, *22*, 227−235.
(56) Iqbal, H. M. N.; Kyazze, G.; Tron, T.; Keshavarz, T. One-pot″ synthesis and characterisation of novel P(3HB)-ethyl cellulose based graft composites through lipase catalysed esterification. *Polym. Chem.* **2014**, *5*, 7004−7012.
(57) Yin, Y. Y.; Lucia, L. A.; Pal, L.; Jiang, X.; Hubbe, M. A. Lipase-catalyzed laurate esterification of cellulose nanocrystals and their use as reinforcement in PLA composites. *Cellulose* **2020**, *27*, 6263−6273.
(58) Knight, E.; Przyborski, S. Advances in 3D cell culture technologies enabling tissue-like structures to be created in vitro. *J. Anat.* **2015**, *227*, 746−756.
(59) Metwally, S.; Stachewicz, U. Surface potential and charges impact on cell responses on biomaterials interfaces for medical applications. *Mater. Sci. Eng., C* **2019**, *104*, 109883.
(60) Misra, S. K.; Mohn, D.; Brunner, T. J.; Stark, W. J.; Philip, S. E.; Roy, I.; Salih, V.; Knowles, J. C.; Boccaccini, A. R. Comparison of nanoscale and microscale bioactive glass on the properties of P(3HB)/Bioglass composites. *Biomaterials* **2008**, *29*, 1750−1761.
(61) Jo, J. H.; Lee, E. J.; Shin, D. S.; Kim, H. E.; Kim, H. W.; Koh, Y. H.; Jang, J. H. In vitro/in vivo biocompatibility and mechanical properties of bioactive glass nanofiber and poly (ε-caprolactone) composite materials. *J. Biomed. Mater. Res., Part B* **2009**, *91*, 213−220.
(62) Lyu, Z.; Wang, H.; Wang, Y.; Ding, K.; Liu, H.; Yuan, L.; Shi, X.; Wang, M.; Wang, Y.; Chen, H. Maintaining the pluripotency of mouse embryonic stem cells on gold nanoparticle layers with nanoscale but not microscale surface roughness. *Nanoscale* **2014**, *6*, 6959−6969.
(63) Park, J.; Bauer, S.; Mark, K.; Schmuki, P. Nanosize and vitality: TiO_2 nanotube diameter directs cell fate. *Nano Lett.* **2007**, *7*, 1686−1691.
(64) Yang, S.; Jang, L.; Kim, S.; Yang, J.; Yang, K.; Cho, S. W.; Lee, J. Y. Polypyrrole/alginate hybrid hydrogels: electrically conductive and soft biomaterials for human mesenchymal stem cell culture and potential neural tissue engineering applications. *Macromol. Biosci.* **2016**, *16*, 1653−1661.
(65) Wan, A. M.-D.; Inal, S.; Williams, T.; Wang, K.; Leleux, P.; Estevez, L.; Giannelis, E. P.; Fischbach, C.; Malliaras, G. G.; Gourdon, D. 3D conducting polymer platforms for electrical control of protein conformation and cellular functions. *J. Mater. Chem. B* **2015**, *3*, 5040−5048.
(66) Guo, B.; Ma, P. X. Conducting polymers for tissue engineering. *Biomacromolecules* **2018**, *19*, 1764−1782.

https://doi.org/10.1021/acsabm.2c00496
ACS Appl. Bio Mater. 2022, 5, 3999−4019